




Optical continuum photometric reverberation mapping of the Seyfert-1 galaxy Mrk509

F. Pozo Nuñez^{1,2,3*} , N. Gianniotis⁴ , J. Blex², T. Lisow², R. Chini^{2,6},
K. L. Polsterer⁴, J.-U. Pott⁵ , J. Esser⁵, and G. Pietrzyński³

¹*Haifa Research Center for Theoretical Physics and Astrophysics, Haifa 31905, Israel*

²*Astronomisches Institut, Ruhr-Universität Bochum, Universitätsstraße 150, 44801 Bochum, Germany*

³*Centrum Astronomiczne im. Mikołaja Kopernika, PAN, Bartycka 18, 00-716 Warsaw, Poland*

⁴*Heidelberg Institute for Theoretical Studies gGmbH, Heidelberg, Germany*

⁵*Max-Planck Institut für Astronomie, Königstuhl 17 Heidelberg, Germany*

⁶*Instituto de Astronomía, Universidad Católica del Norte, Avenida Angamos 0610, Casilla 1280, Antofagasta, Chile*

Accepted 2019 October 3. Received 2019 October 1; in original form 2019 August 29

ABSTRACT

We present the results of a two year optical continuum photometric reverberation mapping campaign carried out on the nucleus of the Seyfert-1 galaxy Mrk509. Specially designed narrow-band filters were used in order to mitigate the line and pseudo-continuum contamination of the signal from the broad line region, while allowing for high-accuracy flux-calibration over a large field of view. We obtained light curves with a sub-day time sampling and typical flux uncertainties of 1%. The high photometric precision allowed us to measure inter-band continuum time delays of up to ~ 2 days across the optical range. The time delays are consistent with the relation $\tau \propto \lambda^{4/3}$ predicted for an optically thick and geometrically thin accretion disk model. The size of the disk is, however, a factor of 1.8 larger than predictions based on the standard thin-disk theory. We argue that, for the particular case of Mrk509, a larger black hole mass due to the unknown geometry scaling factor can reconcile the difference between the observations and theory.

Key words: galaxies: active –galaxies: Seyfert –quasars: emission lines –galaxies: distances and redshifts –galaxies: individual: Mrk509

1 INTRODUCTION

Active galactic nuclei (AGN) are believed to be powered by an accretion disk around a super-massive black hole (SMBH). The strong radiation from the accretion disk photo-ionizes the gas clouds in the broad-line region (BLR) giving rise to the characteristic emission lines observed in the spectrum of quasars and Seyfert galaxies (e.g. Davidson & Netzer 1979). The velocity of the BLR clouds combined with its average distance to the accretion disk can be used to estimate the black hole mass in AGN. The BLR responds to the strong and variable UV/Optical continuum at very short time-scales, and thus at small distances (~ 1 to 250 light days) from the accretion disk. The small distance means that it is very difficult to resolve the central engine of AGN unless several radio telescopes are combined

to create an earth-size detector capable to achieve the high spatial resolution needed (see the reviews by Antonucci 2015 and Netzer 2015). Recent developments in instrumentation allowed to resolve the accretion disk and the BLR system for the particular case of very nearby active galaxies (Gravity Collaboration et al. 2018; Event Horizon Telescope Collaboration et al. 2019). However, it will be impossible to resolve a large sample of more distant AGN in the foreseeable future. Fortunately, in order to estimate black hole masses for a larger sample of objects located at different redshifts, we can resort to the reverberation mapping (RM) method (Cherepashchuk & Lyutyi 1973; Blandford & McKee 1982; Gaskell & Sparke 1986). RM is independent of the spatial resolution of the instrument and relies only on the strong, intrinsic variability to measure the time delay, τ , between changes in the accretion disk continuum and the emission lines from the BLR. This allows estimating the average distance of the BLR clouds to the accretion disk

* E-mail: francisco.pozon@gmail.com

Table 1. Characteristics of Mrk509.

α (2000) ⁽¹⁾	δ (2000) ⁽¹⁾	z ⁽²⁾	D_L ⁽²⁾ (Mpc)	$M_{\text{BH}}^{(3)}$ (M_{\odot})	$\tau_{\text{H}\beta}^{(3)}$ (days)	$\sigma_{\text{H}\beta}^{(3)}$ (km s^{-1})	$A_V^{(3)}$ (mag)
20:44:09.7	-10:43:25.0	0.0344	145.0	$14.3 \pm 1.2 \times 10^7$	$79.6^{+6.1}_{-5.4}$	1276 ± 28	0.309

References: [1] - NED database; [2] - Huchra et al. (1993); [3] - Peterson et al. (2004); The velocity dispersion of the H β emission line ($\sigma_{\text{H}\beta}$) together with the time delay between the optical continuum and the H β emission line ($\tau_{\text{H}\beta}$) were used to estimate M_{BH} .

($R_{\text{BLR}} = c \cdot \tau_{\text{BLR}}$, c is the speed of light). Through the combination of spectroscopic (e.g. ; Peterson et al. 2004; Grier et al. 2012) and photometric monitoring (Haas et al. 2011; Pozo Nuñez et al. 2012; Chelouche & Daniel 2012), the method has revealed the size of the BLR, black hole masses and Eddington ratios in about 100 AGN (e.g. Du et al. 2014, and references therein).

Based on RM measurements of several nearby low-luminosity Seyfert-1 galaxies and a few distant high luminosity quasars, a tight relationship between the accretion disk 5100 Å monochromatic luminosity and the size of the BLR has been established ($R_{\text{BLR}} \propto L_{\text{AD}}^{\alpha}$; Kaspi et al. 2000; Bentz et al. 2009b; Bentz et al. 2013; Du et al. 2016). The radius-luminosity relation has been used to estimate single-epoch black hole masses in larger samples and at different redshifts (e.g. Tilton & Shull 2013; Feng et al. 2014; Ho & Kim 2015; Park et al. 2017). However, it remains unclear what is the physical interplay between the accretion disk and the BLR, and whether BLR continuum contamination could bias the inferred accretion disk optical continuum luminosities (e.g. Chelouche, Pozo Nuñez & Kaspi 2019).

Some models suggest that BLR clouds are the consequence of strong dusty wind formed in colder regions of the accretion disk atmosphere (Czerny & Hryniewicz 2011). The BLR gas can become exposed to the strong irradiation from the central continuum source as they move further away from the disk surface, hence connecting the outer part of the disk with the inner edge of the hot dust distribution (Goad et al. 2012; Czerny 2014; Pozo Nuñez et al. 2014; Ramolla et al. 2018). The dusty wind scenario has been supported with a RM campaign of the circumnuclear hot dust in the Seyfert-1 galaxy NGC 4151 (Schnülle et al. 2015). Recent monitoring of NGC 4151 by Esser et al. (2019) showed evidence of correlated changes between the dust radius and the shape variations of the Pa β BLR emission line, suggesting a common origin for the BLR and the dust clouds which are produced in cooler regions of the accretion disk.

Most of the models assume that AGN have sub-Eddington accretion rates described by the standard thin thermal accretion disk theory (Shakura & Sunyaev 1973). While geometrically thin and optically thick disk models have been able to fit the observed spectral energy distribution (SED) in several AGN (e.g. Kishimoto et al. 2008; Capellupo et al. 2015), there are a number of cases where the results are not satisfactory (e.g. Davis et al. 2007; Kokubo et al. 2014; Shankar et al. 2016).

According to the standard accretion disk theory of Shakura & Sunyaev (1973), the effective temperature of a thin disk changes with its radius and can be expressed as a function of the black hole mass and accretion rate (e.g.

Cackett et al. 2007; Liu et al. 2008; Morgan et al. 2010; Fausnaugh et al. 2016). The radial extent of the accretion disk can therefore be probed by studying the continuum emission at different wavelengths. Similar to the stratification and reprocessing effects observed in the BLR, the radiation from the innermost part of the accretion disk, closer to the SMBH, has the peak of the emission at shorter wavelengths and its variability is observed with a time delay with respect to the outer and cooler parts of the disk which are traced by longer wavelengths. This effect can be interpreted as the light travel time across the accretion disk (e.g. Collier et al. 1998). Therefore, time delays between light curves at different continuum bands provide valuable information about the size ($R_{\text{AD}} \sim c \cdot \tau_{\text{AD}}$) and the temperature stratification across the disk, both crucial parameters to test the standard thin-disk theory in AGN (e.g. Liu et al. 2008; Chelouche 2013).

Accretion disk time delays between the UV-optical bands have been detected for a few AGN over the past years (Wanders et al. 1997; Collier et al. 1998; Oknyanskij et al. 2003; Sergeev et al. 2005; Cackett et al. 2007; Edelson et al. 2015; Fausnaugh et al. 2016). The reported uncertainties are large, likely due to under-sampled light curves. Moreover, a large part of those experiments have been carried out using broad-band filters which can bias the results due to the contribution of the BLR emission. In that context, Pozo Nuñez et al. (2017) has recently introduced a photometric RM experimental design using a specific set of narrow-band filters with the aim to mitigate the BLR emission-line contamination and quantify the effect of the BLR diffuse continuum contribution (Chelouche, Pozo Nuñez & Kaspi 2019).

Collier et al. (1998) found that the observed time delays seems to be consistent with the delay-wavelength relation $\tau \propto \lambda^{4/3}$ predicted by geometrically thin accretion disk models. The absolute disk sizes are, however, larger by a factor of ~ 3 than the expected based on standard thin-disk theory (Sergeev et al. 2005; Shappee et al. 2014; Edelson et al. 2015; Fausnaugh et al. 2016; Jiang et al. 2017; Cackett et al. 2018; but see also Mudd et al. 2018). Interestingly, microlensing studies of luminous lensed quasars have independently reached similar conclusions (Pooley et al. 2006; Pooley et al. 2007; Morgan et al. 2010; Mosquera et al. 2013; Chartas et al. 2016), although the flux ratio of the lensed images are sensitive to the size of the emitting region at a particular wavelength. Moreover, the microlensing technique only allows to study the accretion disk in more distant and high-luminosity quasars, while RM can also study local low-luminosity AGN, especially with smaller telescopes.

Mrk509 is a luminous Seyfert 1 galaxy located at a distance of 145 Mpc and redshift $z = 0.0344$ (Huchra et al. 1993). Due to its high brightness, strong variability and

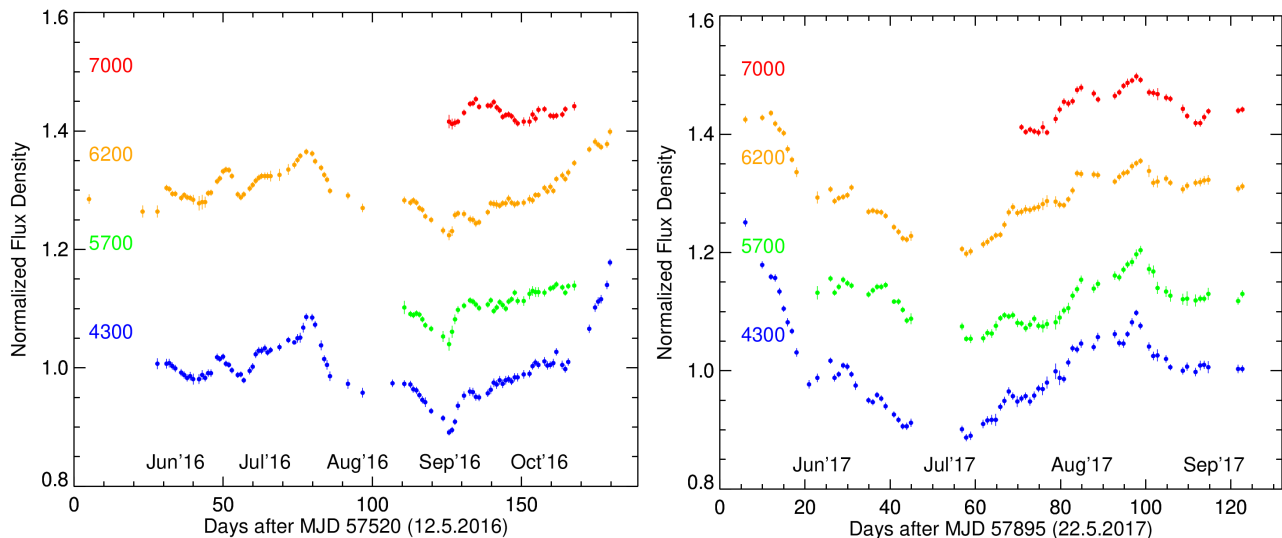


Figure 1. Normalized light curves of Mrk509 for the period between May 2016 and November 2016 (*left*) and for the period between May 2017 and September 2017 (*right*). The light curves are vertically shifted by multiples of 0.2 for clarity.

characteristic outflows, it has been the target of several X-ray/Optical spectroscopic and photometric monitoring campaigns (e.g., Kaastra et al. 2011; Mehdipour et al. 2011; Boissay et al. 2014).

Continuum time delays were observed by Sergeev et al. (2005) who used broad-band *BVRI* variations and attributed the relative lags between the *B* and the *VRI* filters to the light time travel effect and thus to the geometrical size of the region that emits optical continuum.

In this paper, we present the first optical narrow-band continuum photometric reverberation mapping study carried out on the nucleus of Mrk509. We measured continuum time delays using specially designed set of narrow-band filters and discuss the results in the context of emission from an optically thick and geometrically thin accretion disk.

2 OBSERVATIONS AND DATA REDUCTION

The photometric monitoring was conducted between May 17 and November 07, 2016, and between May 05 and September 21, 2017, with the robotic 46 cm telescope of the Wise observatory in Israel. Through Mrk509 redshift of $z = 0.034$, the narrow-bands 4300 ± 50 , 5700 ± 50 , 6200 ± 60 , and 7000 ± 60 Å were used to trace the AGN emission line-free continuum variations. An earlier monitoring carried out in 2014 was performed as part of a RM campaign of the BLR using the robotic 15cm VYSOS-6 and 40cm BMT telescopes located at the Bochum Observatory, near Cerro Armazones in Chile (Blex et al. in prep). The Bochum observations were carried out using the broad-band Sloan-*u* (3609 ± 300) and narrow-band 680 (6800 ± 120) which traces the ultra-violet (UV) continuum variations and the H α emission-line response respectively. Below we discuss details and the implications of the BLR observations (Sect. 4). Figure A1 shows the position of the narrow-band filters together with the spectrum of Mrk509 obtained from the AGN Watch monitoring database (Carone et al. 1996). The characteristics of Mrk509 are summarized in Table 1.

Table 2. Photometric observations.

Filter	λ_{eff}^1 (Å)	F_{Total}^2		No. of observations 2016/2017
		2016/2017 (mJy)		
NB4300	4311	17.11 ± 0.11	17.59 ± 0.12	96/76
NB5700	5688	18.21 ± 0.10	17.41 ± 0.11	42/65
NB6200	6208	21.03 ± 0.12	21.37 ± 0.13	97/74
NB7000	7018	22.69 ± 0.13	23.14 ± 0.13	32/36

¹ Effective central wavelength: $\int \lambda T(\lambda) d\lambda / \int T(\lambda) d\lambda$ where λ is the wavelength and T the filter transmission.

² F_{Total} refer to the mean of the total flux ranges during our monitoring. Fluxes are corrected by galactic foreground extinction.

The images were reduced following standard procedures for image reduction, including bias, dark current, flatfield, astrometry and astrometric distortion corrections performed with IRAF¹ packages and custom written tools, in combination with SWARP (Bertin et al. 2002), SCAMP (Bertin 2006), and Astrometry.net (Lang et al. 2010) routines. A more detailed description of the filters, and data reduction can be found in Pozo Nuñez et al. (2017) for the Wise 46 cm telescope, and in Pozo Nuñez et al. (2015) for the Bochum VYSOS-6 and BMT telescopes.

2.1 Light Curves

The light curves were extracted using image subtraction techniques based on the algorithms implemented in the ISIS

¹ IRAF is distributed by the National Optical Astronomy Observatory, which is operated by the Association of Universities for Research in Astronomy (AURA) under cooperative agreement with the National Science Foundation.

Table 3. Host galaxy and AGN optical fluxes for 2016 and 2017 campaigns.

Filter	Galaxy	AGN ¹
	2016/2017 (mJy)	2016/2017 (mJy)
NB4300	$3.12 \pm 0.72 / 2.94 \pm 0.55$	$13.93 \pm 0.86 / 14.73 \pm 0.75$
NB5700	$7.63 \pm 0.74 / 7.41 \pm 0.56$	$10.62 \pm 0.74 / 10.02 \pm 0.76$
NB6200	$7.93 \pm 0.77 / 7.64 \pm 0.81$	$13.10 \pm 0.88 / 13.73 \pm 0.91$
NB7000	$10.52 \pm 3.01 / 7.81 \pm 0.86$	$12.20 \pm 1.73 / 15.31 \pm 0.94$

package (Alard & Lupton 1998; Alard 2000). The image subtraction procedure together with a comparison with traditional aperture photometry is explained in detail by Pozo Nuñez et al. (2017); here we describe only its main characteristics. First, we construct a reference frame by co-adding the images with the best quality. Then, the reference frame is convolved with a spatially variable kernel to match the point-spread function (PSF) of each individual frame. The convolved reference frame is subtracted from the individual images in order to isolate the AGN variable flux. The final step is the extraction of the nuclear flux which is performed on the resulting difference images using PSF photometry. The quality achieved in the subtracted images allows us to measure the nuclear flux of the AGN with a photometric precision of 0.5% – 1.0%. We also used traditional aperture photometry on the original images in order to compare the performance of both methods. Special care was taken in selecting the aperture that maximizes the signal-to-noise ratio (S/N) and minimize the contribution of the host galaxy. The photometric precision obtained from the aperture photometry is 1.2% – 2.0%. The performance of image subtraction strongly correlates with the quality of the PSF model kernel (Pozo Nuñez et al. 2017), and which in turns depends on the amount of the stars in the field. The field of Mrk509 contains ~ 5000 stars, which is considered a crowded field comparing with Seyfert-1 galaxies located at similar redshifts. This makes image subtraction to outperform aperture photometry in this particular case. The differential fluxes obtained from the image subtraction process are converted to flux units by performing aperture photometry on the reference frame. We find that an aperture of 6.0 arcsec maximizes the S/N and delivered the lowest absolute scatter for the fluxes.

The absolute flux calibration was obtained using the measured fluxes of reference stars from Landolt (2009) observed on the same nights as Mrk509, considering the atmospheric extinction at the Wise observatory and the recalibrated galactic foreground extinction values presented by Schlafly & Finkbeiner (2011). Based on high-resolution stellar templates of our standard stars, we selected only the stars that have moderate absorption around the filter band-passes. We expect that any residual over-estimation of the flux in the bands is $\leq 10\%$. A summary of the photometric results in all bands are listed in Table 2. The normalized light curves for campaigns 2016 and 2017 are shown in Figure 1. The fluxes in all bands are given in tables A1 and A2 in the Appendix.

2.2 Host subtracted AGN luminosity and nuclear reddening

To disentangle the host and AGN contributions to the total flux in the bands, we used the flux variation gradient (FVG) method (Choloniewski 1981; Glass 2004; Sakata et al. 2010; Pozo Nuñez et al. 2014). In brief, the total fluxes obtained through different bands and same apertures follow a linear slope representing the AGN color, while the slope of the host galaxy contribution lies in a well defined range (Sakata et al. 2010). The AGN slope is determined through a bisector linear regression analysis (Isobe et al. 1990). Averaging over the intersection area between the AGN and the host galaxy slopes yields the host galaxy contribution at the time of the monitoring campaign. The FVG diagrams are shown in Figure A2 in the Appendix. The bisector linear regression yields a linear gradient of $\Gamma \sim 1$ during both 2016 and 2017 campaigns. The results are consistent with the gradients obtained for other Seyfert-1 galaxies (Winkler et al. 1992; Sakata et al. 2010). Through the use of high-resolution Hubble Space Telescope images, Bentz et al. (2009b) performed the modeling of the host galaxy profile in Mrk509 and found a bulge morphology type. The host galaxy spectral energy distribution (SED) obtained from the FVG analysis is consistent, within the error margins, with a host bulge model spectrum (Appendix Figure A3).

An important point to consider when isolating the true SED of an AGN is the internal AGN reddening (Gaskell et al. 2004; Gaskell & Benker 2007). Neglecting the effect of nuclear extinction can result in luminosities being underestimated up to a factor of 4 and 10 in the optical and UV respectively (Gaskell 2017). Here, we estimate the nuclear reddening and extinction of Mrk509 directly from the FVG analysis. The bisector method yields a linear gradient of $\Gamma_{4300-5700} = 1.14 \pm 0.06$, by assuming the unreddened or intrinsic color of AGN to be $B - V = 0.0$ ($\Gamma_{BV} = 1.10$ or $\Gamma_{4300-5700} = 1.18$, Winkler et al. 1992; Winkler 1997) we find a nuclear reddening $E(4300 - 5700) = 0.032$, consistent with $E(B - V) = 0.0 \pm 0.02$ found by Winkler et al. (1992) and Winkler (1997) for Mrk509. Considering the AGN reddening curve of Gaskell et al. (2004), the nuclear reddening $E(4300 - 5700) = 0.032$ corresponds to a visual extinction $A_V \sim 0.15$ mag. The intrinsic SED for the nuclear region, after accounting for host galaxy and internal reddening, follows $f_\nu \propto \nu^{1/3}$ (Appendix Figure A3) as predicted for accretion disk models (Shakura & Sunyaev 1973).

The average host galaxy and AGN fluxes obtained in both 2016 and 2017 campaigns are listed in Table 3. Using linear interpolation of the fluxes obtained from the AGN spectrum, we estimate the monochromatic AGN luminosity $\lambda L_{\lambda(\text{AGN})}$ at 5100 \AA to be $L_{\text{AGN}-2016} = (1.63 \pm 0.12) \times 10^{44} \text{ erg s}^{-1}$ and $L_{\text{AGN}-2017} = (1.58 \pm 0.10) \times 10^{44} \text{ erg s}^{-1}$ for campaigns 2016 and 2017 respectively. To determine the luminosities, we used a distance of 145 Mpc (Huchra et al. 1993) assuming a standard cosmology with $H_0 = 73 \text{ km s}^{-1} \text{ Mpc}^{-1}$, $\Omega_\Lambda = 0.73$ and $\Omega_m = 0.27$.

3 TIME SERIES ANALYSIS

In order to robustly estimate the time delays between different continuum bands, we used three different ap-

Table 4. Observed-frame inter-band continuum time delays for 2016 and 2017 campaigns.

Filter	ICCF		DCF		\mathcal{V}_N	
	2016/2017		2016/2017		2016/2017	
	(days)		(days)		(days)	
NB4300	0.00 ^{+0.20} _{-0.20} [1.00]/0.00 ^{+0.20} _{-0.31} [1.00]		0.00 ^{+0.21} _{-0.20} [1.00]/0.00 ^{+0.23} _{-0.30} [1.00]		0.01 ^{+0.21} _{-0.19} /0.00 ^{+0.21} _{-0.33}	
NB5700	0.92 ^{+0.11} _{-0.36} [0.77]/1.12 ^{+0.82} _{-0.92} [0.82]		0.95 ^{+0.10} _{-0.40} [0.77]/1.10 ^{+0.81} _{-1.03} [0.82]		0.96 ^{+0.18} _{-0.42} /1.03 ^{+0.98} _{-1.01}	
NB6200	1.90 ^{+0.71} _{-0.72} [0.89]/1.72 ^{+0.12} _{-0.56} [0.93]		1.81 ^{+0.70} _{-0.73} [0.88]/1.72 ^{+0.12} _{-0.61} [0.93]		1.82 ^{+1.02} _{-0.57} /1.71 ^{+0.49} _{-0.52}	
NB7000	1.89 ^{+1.20} _{-1.22} [0.73]/2.11 ^{+0.61} _{-0.46} [0.74]		1.99 ^{+1.19} _{-1.21} [0.75]/2.10 ^{+0.60} _{-0.41} [0.74]		2.10 ^{+1.12} _{-0.96} /2.01 ^{+0.48} _{-0.28}	

Notes: The maximum correlation coefficient R_{max} is given in parenthesis for both ICCF and DCF methods.

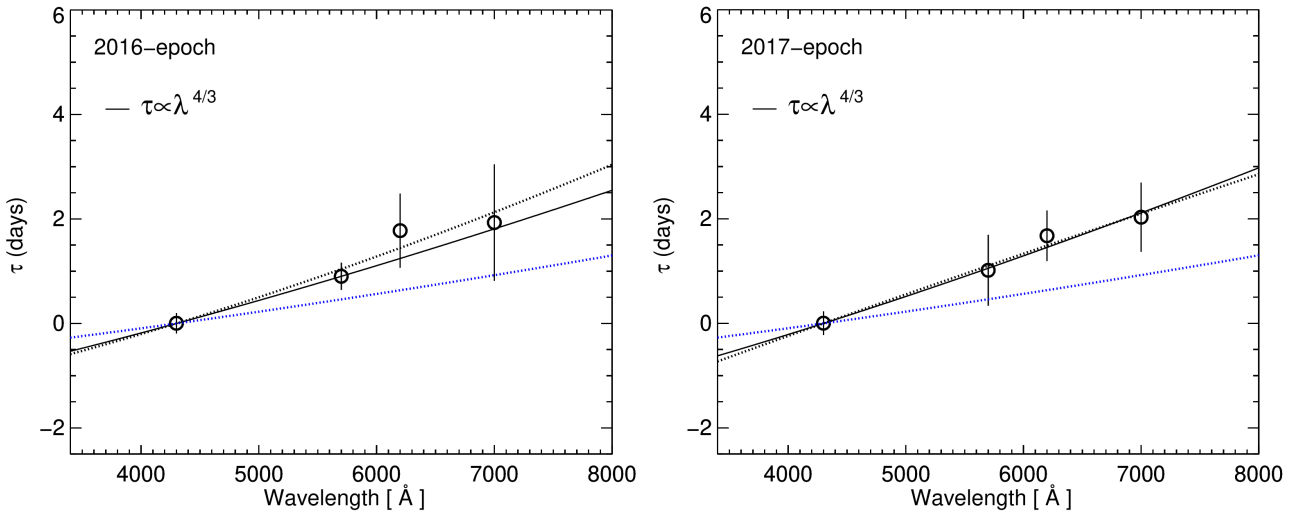


Figure 2. Time delay as a function of wavelength (black open circles) for campaigns 2016 (*left*) and 2017 (*right*). The expected time delays for an optically thick and geometrically thin accretion disk model are shown by the dotted blue lines. The dotted black line shows the best fit to the observed relation $\tau_{jk} = \alpha(\lambda_k^\beta - \lambda_j^\beta)$ with α and β free parameters. The solid black line is the fit with a fixed theoretically expected index $\beta = 4/3$. The time delays are calculated with respect to the 4300 Å narrow-band and are corrected by the time dilation factor ($1+z = 1.0344$).

proaches; the traditional interpolated cross-correlation function (ICCF, Gaskell & Peterson 1987; Kaspi et al. 2000; Peterson et al. 2004), the discrete correlation function (DCF, Edelson & Krolik 1988) including the Z-transformed DCF (Alexander 1997), and the recently introduced von Neumann statistical estimator (VN; Chelouche, Pozo Nuñez & Zucker 2017); the latter one does not rely on interpolation and binning of the light curves but on the level of randomness of the data. Since the VN estimator is not widely known in RM analysis, we give some comprehensive explanations here.

First we create a combined time series F between the driving F_1 and time-delayed F_2^τ continuum light curves so that $F(t, \tau) = \{(t_i, f_i)\}_{i=1}^N = F_1 \cup F_2^\tau$, with $F_2^\tau = \{(t_i + \tau, f_i)\}_{i=1}^{N_2}$, f_i the fluxes measured at times t_i for each of the light curves and $N = N_1 + N_2$ correspond to the total number of data points. The VN estimator of the randomness of the combined light curve is defined as the mean-square of successive differences,

$$\mathcal{V}_N(\tau) = \frac{1}{N-1} \sum_{i=1}^{N-1} \frac{[F(t_i) - F(t_{i+1})]^2}{W_{i,i+1}} \quad (1)$$

where $W_{i,i+1} = 1/[\sigma_{lc}^2(t_i) + \sigma_{lc}^2(t_{i+1})]$ is a weighting factor introduced by Pelt et al. (1994) which takes into account the flux uncertainty (σ_{lc}) from the light curves (see Chelouche, Pozo Nuñez & Zucker (2017) for a slightly modified version of this factor). The goal is to find a time delay τ_0 from a pre-defined search interval $[\tau_{min}, \tau_{max}]$ that will minimize the VN estimator so that $V_N(\tau_0) \equiv \min[V_N(\tau)]$.

For the three methods we used a common time-delay search interval $[\tau_{min}, \tau_{max}] = [-10, 10]$ days, and we estimated the delays relative to the 4300 Å narrow-band. For the ICCF, we used the search interval spaced by 0.1 days, while the DCF was evaluated using a bin size of one day which corresponds to the median sampling of the light curves. Since the light curves are very well sampled, the choice of a lower or higher time-bin size does not change the results. For the ICCF and DCF we estimated the time delay using the centroid τ_{cen} of the cross-correlation function $R(\tau)$

computed above the correlation level at $R \geq 0.7R_{max}$, except for the pairs 4300/7000 in campaign 2017, where we used $R \geq 0.6R_{max}$ due to the lower correlation found between the bands.

Uncertainties in the time delay were calculated using the flux randomization and random subset selection (FR/RSS) method of Peterson et al. (2004) considering the improvements presented by Welsh (1999). From the observed light curves we create 2000 randomly selected subset light curves, each containing 63% of the original data points due to the non-selection of points according to Poisson probability. The flux value of each data point was randomly altered consistent with its normal-distributed measurement error. We calculated the ICCF and DCF for the 2000 pairs of subset light curves and used the 68% confidence range to estimate the errors of the centroid. The time delay measurements obtained by various methods are shown in Figure A4 in the Appendix. Table 4 gives the centroid and the central 68% confidence intervals of the distributions obtained from the FR/RSS method. The time delays obtained with different methods yield consistent results for both 2016/2017 campaigns, although the errors decreased during 2017 campaign due to the higher time sampling of the light curves.

4 DISCUSSION

In the following section, we discuss the results in the context of emission from an optically thick and geometrically thin accretion disk.

4.1 Photometric reverberation mapping of the accretion disk

According to the standard disk theory of Shakura & Sunyaev (1973), the energy flux radiated, due to a viscous heating process, from a surface unit of an optically thick and geometrically thin accretion disk is

$$\mathcal{E}_\nu(R) = \frac{3GM\dot{M}}{8\pi R^3} \left[1 - \left(\frac{R_0}{R} \right)^{1/2} \right] \quad (2)$$

where R is the distance away from the innermost radius R_0 of the disk, G is the gravitational constant, M is the mass of the black hole and \dot{M} the mass accretion rate of the disk. The boundary of the disk is assumed here to be located at R_0 , also referred as the radius of the innermost stable circular orbit around the black hole and for which only the critical flux of the matter can go under $R_0 \sim 3R_g$ with $R_g = 2GM/C^2$ the Schwarzschild radius. Apart from a viscous heating process, the disk photosphere is irradiated by an external UV/X-ray-emitting source with luminosity L_* . Since the geometry of the emitting source is unknown, a simplistic approximation is made by placing the source at a height H_* along the rotational axis of the black hole (see Fig.3 in Sergeev et al. 2005). Considering the albedo a of the disk, the irradiated flux can be expressed as

$$\mathcal{E}_\mathcal{G}(R) = \frac{L_*(1-a)}{4\pi R^3} H_* \cos \theta \quad (3)$$

with θ the angle between the disk surface normal and the incoming radiation of the emitting source (Netzer 2013). The total observed flux from the accretion disk is therefore $\mathcal{E}(R) = \mathcal{E}_\nu(R) + \mathcal{E}_\mathcal{G}(R)$. If the radius R is much greater than the innermost radius ($R \gg R_0$) and assuming that the local emission is described by a perfect blackbody so that $\mathcal{E} = \sigma T^4$, the temperature across the disk is

$$T(R) = \left[\frac{3GM\dot{M}}{8\pi R^3 \sigma} + \frac{L_*(1-a)}{4\pi R^3 \sigma} H_* \cos \theta \right]^{1/4} \quad (4)$$

The combined temperature profile $T \propto R^{-3/4}$ is responsible for the thermal radiation emitted over a range of wavelengths centred at $\lambda_0 = xhc/kT(R)$, where x is a factor needed in the conversion from T to λ for a given radius R . Since the factor x depends on the function that is used to describe the radius response to the emitted radiation, we set $x = 2.49$ obtained by adopting a flux-weighted mean radius $\langle R \rangle = \int_{R_0}^{\infty} B(T(R)) R^2 dR / \int_{R_0}^{\infty} B(T(R)) R dR$ (Fausnaugh et al. 2016; Edelson et al. 2017), with $B(T(R))$ the Planck function, and assuming the temperature profile described in Equation (4). The variable radiation from the innermost part of the disk, closer to the black hole, will have the peak of the emission at shorter wavelengths and due to reprocessing effects, the variability is observed with a time delay τ with respect to the outer and cooler parts of the disk which are traced by longer wavelengths. This effect can be interpreted as the light travel time across the disk so that $\tau = R/c$. In consequence, for two different continuum light curves with central wavelengths at λ_j and λ_k , the predicted time delay τ_{jk} between the bands is given by

$$\tau_{jk} = \gamma \left[\lambda_k^{4/3} - \lambda_j^{4/3} \right] \left[\frac{3GM\dot{M}}{8\pi\sigma} + \frac{L_*(1-a)}{4\pi\sigma} H_* \cos \theta \right]^{1/3} \quad (5)$$

with $\lambda_k > \lambda_j$, and $\gamma = c^{-1}(xk/hc)^{4/3}$. We note that a simplified version of Equation (5) can be obtained by assuming that the ratio of external to internal heating of the disk ($\kappa = 2L_*(1-a)H_*/GMM$) is close to zero, i.e. the contribution of the external UV/X-ray radiation above the disk plane $\mathcal{E}_\mathcal{G}$ (Equation 3) is negligible compared to internal viscous dissipation (see Equation [5] of Collier et al. 1998 and Equation [3] of Edelson et al. 2017).

Figure 2 shows the rest-frame average time delay as a function of the central wavelength ($\lambda_0/[1+z]$ in Angstroms) obtained for both 2016 and 2017 campaigns. We fit the time delays with the model $\tau_{jk} = \alpha(\lambda_k^\beta - \lambda_j^\beta)$ with α and β as free parameters. The best fit for campaign 2016 is obtained with $\alpha = 2.27 \pm 0.48$ days and $\beta = 1.48 \pm 0.61$ and with $\alpha = 2.11 \pm 0.36$ days and $\beta = 1.21 \pm 0.42$ for campaign 2017. We then fix $\beta = 4/3$ in order to test the time delay-wavelength relation as predicted for an optically thick and geometrically thin accretion disk model. The best fit is obtained with $\alpha = 2.07 \pm 0.28$ days for 2016 and $\alpha = 2.16 \pm 0.19$ for 2017. The measured rest-frame delays can be well-fitted by the standard disk model $\tau \propto \lambda^{4/3}$ in both observing campaigns, albeit with lower uncertainties for both α ($\sim 17\%$) and β ($\sim 35\%$) parameters during 2017 monitoring. This is expected because of the higher time-sampling obtained for the light curves in 2017 (~ 0.8 days) which leads to improved time delay measurements with lower average uncertainties.

4.2 The accretion disk size of Mrk509

The observed continuum time delays can be compared with those expected from the standard disk theory for a given black hole mass and mass accretion rate. Assuming a bolometric luminosity correction $L_{\text{Bol}} = 10\lambda L_{\lambda}(5100\text{\AA})$ (McLure & Dunlop 2004), a black hole mass of $M = 14.3 \pm 1.2 \times 10^7 M_{\odot}$ (Peterson et al. 2004), and a mass to radiation conversion efficiency $\eta = L_{\text{Bol}}/\dot{M}c^2 = 0.10$ (Shankar et al. 2009), we estimate the mass accretion rate $\dot{M}_{2016} = 0.29 M_{\odot} \text{yr}^{-1}$ and $\dot{M}_{2017} = 0.28 M_{\odot} \text{yr}^{-1}$ for 2016 and 2017 campaigns respectively. The AGN luminosity did not change between the two years, hence the mass accretion rate remained constant. During an XMM-Newton monitoring carried out in 2011 focusing on Mrk509, Mehdipour et al. (2011) estimated a range for the mass accretion rate of $0.24 \leq \dot{M} \leq 0.34 M_{\odot} \text{yr}^{-1}$. Their average value $\langle \dot{M} \rangle = 0.29 M_{\odot} \text{yr}^{-1}$ is exactly the same as the average value we obtained for 2016 and 2017 campaigns.

Given our determination of the mass accretion rate and the black hole mass, we calculate the expected rest-frame time delay with respect to the reference wavelength 4300 Å (Equation [5]) to be $\tau = 1.16$ days. Our measured rest-frame delay is a factor of 1.8 larger than the predicted by the standard disk model. An explanation for such a discrepancy could be that the black hole mass of Mrk509 is underestimated. The black hole mass reported by Peterson et al. (2004) has been calculated assuming a geometry-scaling factor $f = 5.5$ (Onken et al. 2004). The UV continuum and H α emission-line variability observed during 2014 campaign revealed that the echo of the BLR has a mean lag of ~ 35 days (Blex et al. in prep). In order to constrain the f value from the BLR data, we modelled the H α light curve assuming Keplerian orbits, thin/thick disks and spherical BLR geometries. The modelling follows that of Pozo Nuñez et al. (2014). The convolution of the UV continuum light curve with a thin-disk BLR model at inclination $i = 12^{\circ}$ provides an acceptable fit to the observed H α data (Figure 3). If the BLR of Mrk509 has a nearly face-on disk-like BLR geometry, the geometry-scaling factor is $f = \frac{2 \ln 2}{\sin^2 i} = 32$. This is about 6 times larger than the commonly used average value obtained by Onken et al. (2004), and which assumes that AGN and quiescent galaxies follow the same $M_{\text{BH}} - \sigma_*$ relationship. Therefore, if we adopt $f = 32$ it results in a black hole mass of $M \sim 8 \times 10^8 M_{\odot}$. In the next section, we describe the implications of the thin-disk BLR geometry for the observed time delays.

4.2.1 Accretion disk probabilistic modelling

We carry out a probabilistic analysis in order to explore the set of likely solutions for the thin AD model $\tau \propto \lambda^{4/3} (MM)^{1/3}$ whose geometry constrains the black hole mass M (Figure 3).

We set the velocity dispersion of the H α emission-line to $V_{\text{H}\alpha} = 1730 \pm 400 \text{ km/s}$ (Blex et al. in prep), and the mass accretion rate to $\dot{M} = L_{\text{Bol}}/\eta c^2$, assuming a bolometric correction $L_{\text{Bol}} = 10\lambda L_{\lambda}(5100\text{\AA})$. Since the radiative efficiency η depends on the spin of the black hole, we set $\eta = 0.1$ which assumes that the black hole is co-rotating with the disk².

² The radiative efficiency η can vary between 0.038 and 0.42 de-

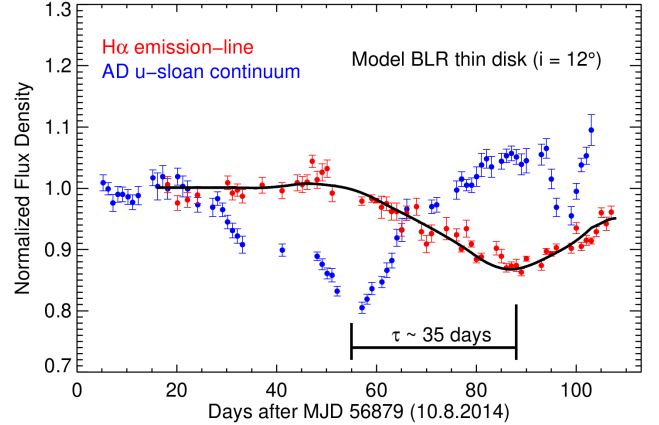


Figure 3. BLR thin-disk model. The blue and red dots show the observed (host-galaxy corrected) UV continuum and H α light curves respectively. A thin-disk BLR model (black solid line) that extends from 32 to 43 light days and has an inclination $i = 12^{\circ}$ is able to reproduce the features of the H α light curve.

Under the previous assumptions, we define the time-delay function $\phi \propto \lambda^{4/3} (\sin^{-2}(i) R_{\text{BLR}} V_{\text{H}\alpha}^2 L_{5100\text{\AA}})^{1/3}$, where the free model parameters are $\theta = (i, R_{\text{BLR}}, L_{5100\text{\AA}})$. The observed data $\mathcal{D} = \{(\tau_n, \sigma_n, \lambda_n)\}_{n=1}^N$ are taken from the 2017 campaign (Table 4). The goal of this analysis is to infer the posterior distribution $p(\theta|\mathcal{D})$ of the thin AD model parameters. This distribution will help us to examine whether the observed data support our BLR geometry assumption which attempts to reconcile the apparent discrepancy between observed and theoretical time delays.

We formulate the following probabilistic model via the likelihood function $p(\mathcal{D}|\theta)$:

$$\begin{aligned} p(\mathcal{D}|\theta) &= \prod_{n=1}^N p(\tau_n | \lambda_n, i, R_{\text{BLR}}, L_{5100\text{\AA}}, \sigma_n) \\ &= \prod_{n=1}^N \mathcal{N}(\tau_n | \phi_{\text{rel}}(\lambda_n; i, R_{\text{BLR}}, L_{5100\text{\AA}}), \sigma_n) \end{aligned} \quad (6)$$

where $\mathcal{N}(x|a, b)$ is the normal distribution with mean and standard deviation a and b respectively. The mean of the normal distributions in Equation [6] is given by the delay-wavelength relation relative to 4300Å:

$$\begin{aligned} \phi_{\text{rel}}(\lambda_n; i, R_{\text{BLR}}, L_{5100\text{\AA}}) &= \phi(\lambda_n; i, R_{\text{BLR}}, L_{5100\text{\AA}}) \\ &\quad - \phi(4300\text{\AA}; i, R_{\text{BLR}}, L_{5100\text{\AA}}) \end{aligned} \quad (7)$$

We complete the probabilistic formulation by imposing prior distributions on the model parameters $p(\theta) = p(i) p(R_{\text{BLR}}) p(L_{5100\text{\AA}})$ with $p(i) = \mathcal{U}(i|0.0^{\circ}, 40.0^{\circ})$ and $p(R_{\text{BLR}}) = \mathcal{U}(R_{\text{BLR}}|10.0, 100.0 \text{ days})$ where $\mathcal{U}(x|a, b)$ is the continuous uniform distribution with support $[a, b]$. Regarding luminosity, we impose the normal prior $p(L_{5100\text{\AA}}) = \mathcal{N}(L_{5100\text{\AA}} | 1.5761068 \times 10^{44}, 0.10 \times 10^{44} \text{ erg s}^{-1})$

pending on the spin of the black hole (Davis & Laor 2011). A value of $\eta \geq 0.1$ is commonly used for co-rotating disks, smaller or larger values will underestimate/overestimate the mass accretion rate.

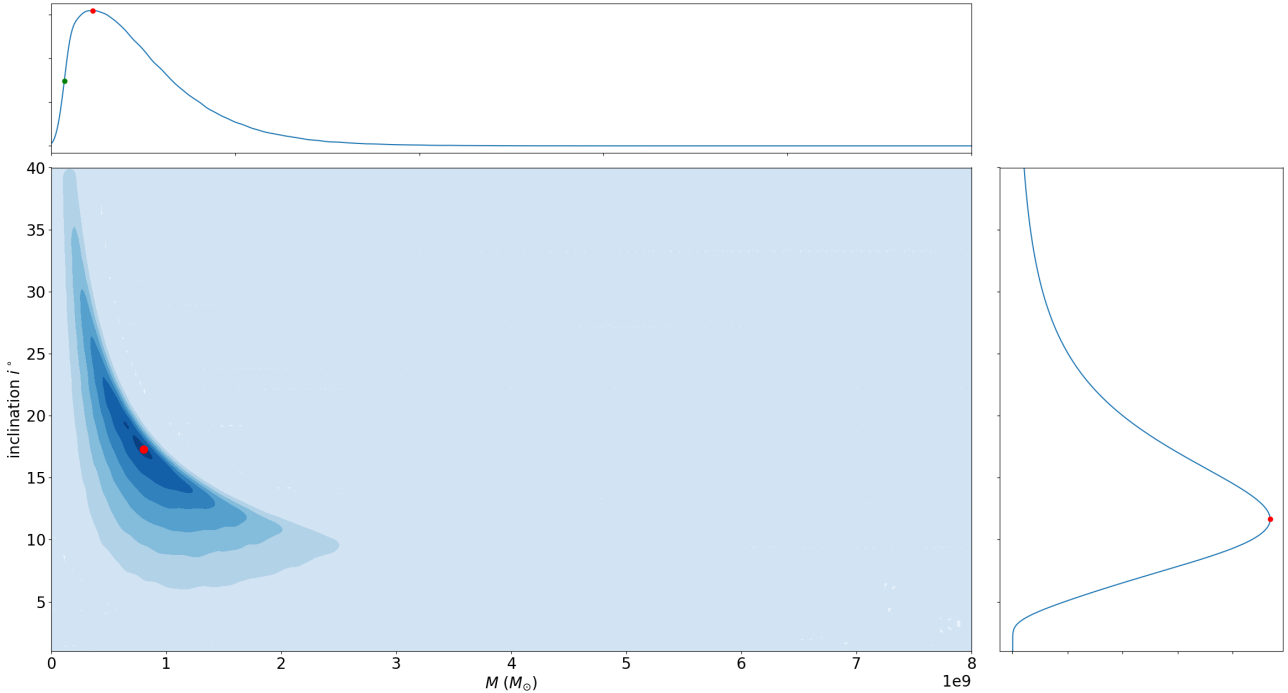


Figure 4. Posterior distribution for mass-inclination $p(M, i | \mathcal{D})$. The plot shows how much the data support M, i pairs as candidate solutions; the stronger the hue, the more likely the pair. The marginal $p(i | \mathcal{D})$ (top) shows the distribution of i after accounting of the effect of all other model parameters. Similarly, we show the marginal $p(M | \mathcal{D})$ at the right. While the most likely pair is the pair $M = 7.82 \times 10^8 M_{\odot}, i = 17.49^{\circ}$, shown as a red dot in the $p(M, i | \mathcal{D})$ diagram, the posterior reveals that other pairs are also probable. We note that in general, the mode of the joint distribution does not coincide with the mode of the marginals. An indication of the range of probable distinct values for i and M can be read in the marginal distributions, with the most likely value also marked as a red dot for each case. Additionally, we plot as a green dot the previous estimate for the mass $M = 14.3 \pm 1.2 \times 10^7 M_{\odot}$ which under our probabilistic analysis now appears as a less likely estimate.

informed by the luminosity obtained in the 2017 campaign (Section 2.2).

The joint posterior of the model parameters is given by Bayes' theorem³:

$$p(\theta | \mathcal{D}) = \frac{p(\mathcal{D} | \theta) p(\theta)}{\int p(\mathcal{D} | \theta) p(\theta) d\theta} \quad (8)$$

Our aim is to verify whether the hypothesis of a BLR thin-disk geometry with a low inclination i and an upwards revised estimate for the mass M , is consistent with the observed data. Hence, the specific quantity we seek to infer is the joint distribution $p(M, i | \mathcal{D})$. This can be computed numerically by first drawing a large number of samples from the posterior

$$i, R_{\text{BLR}}, L_{5100\text{\AA}} \sim p(i, R_{\text{BLR}}, L_{5100\text{\AA}} | \mathcal{D}) = p(\theta | \mathcal{D}) \quad (9)$$

Samples for the mass parameter M are indirectly obtained from the drawn R_{BLR}, i samples. Having obtained a large number of samples, we then use kernel density estimation to estimate $p(M, i | \mathcal{D})$ from the drawn samples. Figure 4 shows the estimated posterior probability $p(M, i | \mathcal{D})$ along with the marginals $p(i | \mathcal{D})$ and $p(M | \mathcal{D})$. It is evident that

³ In order to compute the posterior, we discretize the support of each physical parameter on a grid of 400 number of equidistant grid points. This turns the integrals into easily computable sums. While this numerical approach is feasible for our case of three model parameters, it is impractical for more parameters.

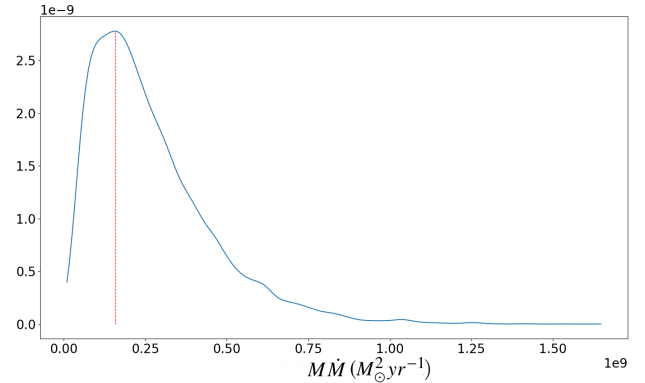


Figure 5. Probability distribution for MM . The vertical dotted line marks the mode $MM = 1.58 \times 10^8 M_{\odot}^2 \text{yr}^{-1}$ of the distribution.

the black hole mass obtained with a geometry-scaling factor $f = 5.5$ ($M = 14.3 \pm 1.2 \times 10^7 M_{\odot}$) is a less likely estimate. The marginal $p(i | \mathcal{D})$ reveals that likely inclinations are roughly in the range $10^{\circ} \leq i \leq 30^{\circ}$; $p(M | \mathcal{D})$ reveals that black hole masses are roughly in the range $0.2 \leq M \leq 1.5 \times 10^9 M_{\odot}$. The mode of the marginal distribution for the inclination and black hole mass is $i = 11.65^{\circ}$ and $M = 4.77 \times 10^8 M_{\odot}$ respectively. These values are in good agreement with the point estimates derived from the BLR modelling (Figure 3).

We compute also the probability distribution $p(MM)$

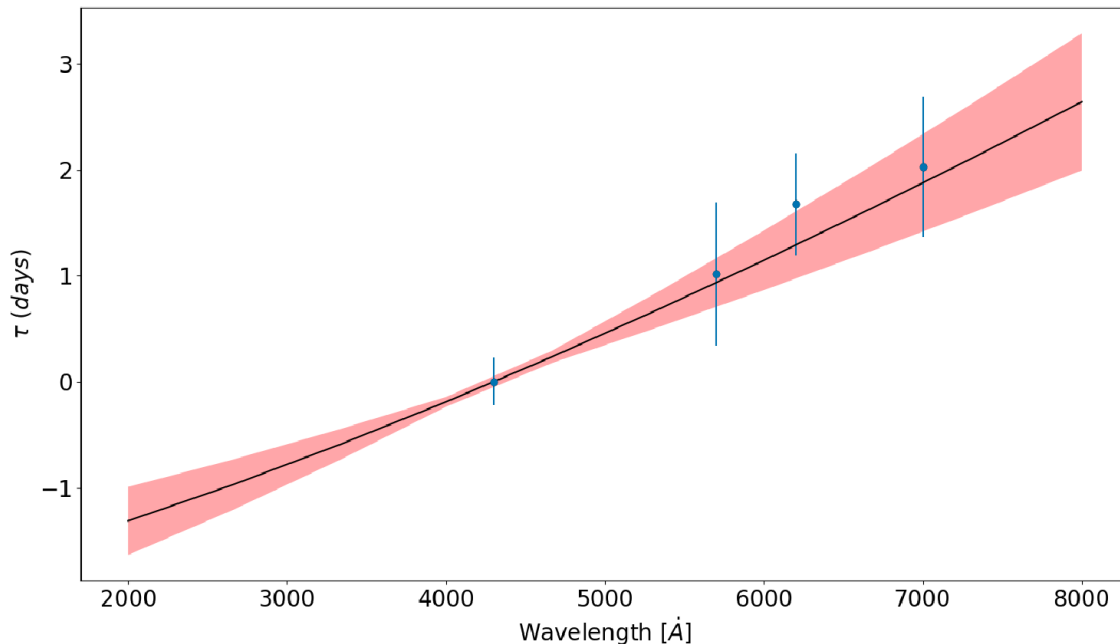


Figure 6. Predictive distribution of AD models along with the data from the 2017 campaign. The black line is the mean of this distribution (i.e. the mean prediction), while the red shaded area corresponds to ± 1 standard deviation from the mean.

(Figure 5). The most likely value for the product is $M\dot{M} = 2.2 \times 10^8 M_{\odot}^2 \text{yr}^{-1}$. If we consider the mode obtained from the marginal distribution for the black hole mass, the accretion rate is $\dot{M} = 0.33 M_{\odot} \text{yr}^{-1}$, which is consistent with the average value $\langle \dot{M} \rangle = 0.29 M_{\odot} \text{yr}^{-1}$ obtained for 2016 and 2017 campaigns. Figure 6 plots the posterior predictive distribution for the AD models $p(\tau|\lambda) = \int p(\tau|\lambda; \theta) p(\theta|\mathcal{D}) d\theta$ as supported by the posterior $p(\theta|\mathcal{D})$. In other words, the plot reveals the distribution of the AD model predictions as weighted by the posterior $p(\theta|\mathcal{D})$. The new estimate of M and \dot{M} , obtained for a thin-disk BLR at inclination $i = 12^\circ$, increase the accretion disk size to ~ 2 days⁴, hence consistent with our observations.

Recent continuum reverberation mapping studies have also found accretion disk sizes which are a factor of $\sim 2 - 3$ larger than predicted by the standard thin disk model (NGC5548; Edelson et al. 2015, and Fausnaugh et al. 2018 for the Seyfert-1 galaxies NGC2617 and MCG+08-11-011). These previous studies have been carried out using broadband filters which are contaminated by emission from the BLR and therefore they might bias the time delays to larger values. As shown by Edelson et al. (2015) for NGC5548, the observed U-band time-delay of 1.35 days versus a predicted delay of 0.85 days can be explained by accounting for

⁴ It is clear from Equation (5) that not only a larger value for the black hole mass will result in a larger disk size, for instance, if we assume that all the emission at a certain wavelength comes from an annulus of radius R at a temperature given by Wien's law, the factor x becomes twice as large (4.97), increasing the γ factor in Equation (5) and scaling the disk size by a factor ~ 2.5 . However, the use of a flux-weighted radius is a more realistic assumption since it assumes that the temperature profile of the disk follows $T \propto R^{-3/4}$ as predicted by the standard disk theory of Shakura & Sunyaev (1973).

Balmer diffuse continuum emission from the BLR, hence the advantage of using narrow-band filters which are less affected by BLR emission. Another interesting example is NGC2617 ($z = 0.014$) for which Fausnaugh et al. (2018) found a disk size about 2.1 larger than predicted. NGC2617 is about 40 times less luminous than Mrk509 and the authors were able to account for the systematic difference by increasing the product $M\dot{M}$, although they did not account for a larger black hole mass due to BLR geometry effects.

Gaskell (2017) proposed that the larger accretion disk sizes found by previous RM and microlensing studies can be reconciled with the standard disk theory (Shakura & Sunyaev 1973) after correcting for AGN internal extinction. Accounting for AGN reddening can increase the optical $L_{5100\text{\AA}}$ luminosities up to a factor of 4. However, as shown in Section 2.2, Mrk509 has a reddening consistent with $E(B-V) = 0$ and therefore nuclear extinction does not explain the observed larger disk size.

Using the same filter configuration than for Mrk509, Chelouche, Pozo Nuñez & Kaspi (2019) found significantly larger continuum time delays for the Seyfert-1 galaxy Mrk279. The delays observed in Mrk279 followed a supralinear steep rise with wavelength, implying a different temperature profile than the predicted by the standard thin-disk theory. From reported lags of 14 AGN, Gaskell (2007) observed a similar steep rise in τ at long wavelengths. He attributed this to contamination by light being reprocessed from further away. For Mrk279 and the objects considered by Gaskell (2007), the steep rise observed in the time-delay with wavelength is a consequence of emission of a farther away, under-appreciated, non-disk component that significantly contributes to the flux at longer wavelengths. Through the use of photo-ionization modelling, Chelouche, Pozo Nuñez & Kaspi (2019) identify this component as high-density, photo-ionized material that has been uplifted from the outer ac-

tion disk, likely due to radiation-pressure force on dust. This supra-linear steep rise with wavelength found in Mrk279 has not been found in Mrk509 and therefore the observed uplifted material from the accretion disk is particularly related to the source.

5 CONCLUSIONS

We have performed a two-year photometric reverberation mapping monitoring campaign in order to study the optical continuum emission from the nucleus of the Seyfert-1 galaxy Mrk509. The main results are:

(i) We have detected inter-band continuum time delays in two different epochs 2016 and 2017 by using a novel narrow-band imaging experimental design which mitigates the emission line and pseudo-contamination of the signal from the BLR. The results are remarkably consistent between both photometric campaigns, although the time-delay measurements have been improved significantly in 2017 as a consequence of the higher (sub-day) time sampling obtained for the light curves. The measurements are also consistent with the fact that the average bolometric luminosity remained constant during both observing campaigns. These results confirm that time resolution is a crucial factor in order to measure AGN continuum time delays with an accuracy needed to constrain theoretical models of the accretion disk, therefore future coordinated ground-based optical observing campaigns are of vital importance.

(ii) the time delays increase with wavelength according to the relation $\tau \propto \lambda^{4/3}$ predicted for an optically thick and geometrically thin accretion disk. However, the inferred disk size is larger by a factor of 1.8 than predictions based on the standard thin-disk theory.

(iii) the larger disk size found in Mrk509 can be explained if the black hole mass is a factor of 3.3 larger than the current value obtained through reverberation mapping of the BLR. This is supported with a probabilistic modelling of the continuum time delays that assumes a BLR with a thin-disk like geometry, and independently corroborated by the direct modeling of the BLR observations. The BLR small inclination $i \sim 12^\circ$ leads to a geometry-scaling factor f that is ~ 6 times larger than the commonly used average value ($f = 5.5$). The internal extinction and bolometric luminosity corrections plays a minor role in the particular case of Mrk509.

(iv) the accretion disk probabilistic modelling of the continuum time delays can be used directly to infer the black hole masses without explicitly accounting for the BLR geometry scaling factor. In that way, the resulting black hole masses can be compared with values obtained by the direct modeling of the BLR emission-line light curves. Since this is clearly a model dependent analysis, it can only be applied if the data are not biased by the effect of inclination or external contamination (e.g. AGN internal reddening, BLR line and diffuse continuum emission), highlighting the importance of using specific designed narrow-band filters. Future applications of this approach on larger data sets will provide more constraints on specific models of the accretion disk.

Although in some cases the black hole masses might

not fully reconcile the theory with observations, their uncertainties due to the unknown geometry of the BLR are still important quantities that need to be improved. Microlensing studies have reported larger accretion disk sizes for luminous distant quasars, however, high redshift-quasars have a factor of 10 higher black hole masses than quiescent galaxies, hence a scaling factor f obtained from the $M_{BH} - \sigma_*$ relationship may not be valid in general. Whether a BLR with a thin-disk like structure holds for all Seyfert-1 galaxies, the determination of the f -factor is crucial in order to constrain the significance of the discrepancies between observations with the standard accretion disk theory. In that context, coordinated ground-based optical monitoring campaigns of the accretion disk and the BLR are necessary to increase the observing time-sampling needed to study specific accretion disk models and to further decrease the biases in the time-delay measurements.

ACKNOWLEDGEMENTS

We are grateful to D. Maoz and D. Chelouche for allowing the use of the C18 telescope in Israel, and S. Kaspi for providing technical support with C18 telescope operation. We thank M. Murphy for providing technical support with the telescope operations at the Cerro Armazones observatory in Chile. This research has been partly supported by grants 950/15 from the Israeli Science Foundation (ISF) and 3555/14-1 from the Deutsche Forschungsgemeinschaft (DFG). We also acknowledge support from the IdP II 2015 0002 64 and DIR/WK/2018/09 grants of the Polish Ministry of Science and Higher Education. This work is based on observations collected at the Wise Observatory with the C18 telescope. The C18 telescope and most of its equipment were acquired with a grant from the Israel Space Agency (ISA) to operate a Near-Earth Asteroid Knowledge Center at Tel Aviv University. Authors N.G and K.L.P gratefully acknowledge the generous and invaluable support of the Klaus Tschira Foundation. This work was supported by the Nordrhein-Westfälische Akademie der Wissenschaften und der Künste, funded by the Federal State Nordrhein-Westfalen and the Federal Republic of Germany. This research has made use of the NASA/IPAC Extragalactic Database (NED) which is operated by the Jet Propulsion Laboratory, California Institute of Technology, under contract with the National Aeronautics and Space Administration. This research has made use of the SIMBAD database, operated at CDS, Strasbourg, France. We thank our referee Martin Gaskell for his constructive comments and careful review of the manuscript.

REFERENCES

- Alard, C., & Lupton, R. H. 1998, ApJ, 503, 325
- Alard, C. 2000, A&AS, 144, 363
- Alexander, T. 1997, Astronomical Time Series, 218, 163
- Antonucci, R. 2015, arXiv:1501.02001
- Bentz, M. C., Walsh, J. L., Barth, A. J., et al. 2009b, ApJ, 705, 199
- Bentz, M. C., Denney, K. D., Grier, C. J., et al. 2013, ApJ, 767, 149

- Bertin, E., Mellier, Y., Radovich, M., et al. 2002, *Astronomical Data Analysis Software and Systems XI*, 281, 228
- Bertin, E. 2006, *Astronomical Data Analysis Software and Systems XV*, 351, 112
- Blandford, R. D. & McKee, C. F. 1982, *ApJ*, 255, 419
- Boissay, R., Paltani, S., Ponti, G., et al. 2014, *A&A*, 567, A44.
- Capellupo, D. M., Netzer, H., Lira, P., Trakhtenbrot, B., & Mejía-Restrepo, J. 2015, *MNRAS*, 446, 3427
- Carone, T. E., Peterson, B. M., Bechtold, J., et al. 1996, *ApJ*, 471, 737
- Chartas, G., Rhea, C., Kochanek, C., et al. 2016, *Astronomische Nachrichten*, 337, 356
- Chelouche, D., & Daniel, E. 2012, *ApJ*, 747, 62
- Chelouche, D. 2013, *ApJ*, 772, 9
- Chelouche D., Pozo-Núñez F., Zucker S., 2017, *ApJ*, 844, 146
- Chelouche D., Pozo Nuñez F., Kaspi S., 2019, *NatAs*, 3, 251
- Choloniewski, J. 1981, *Acta Astron.*, 31, 293
- Cherepashchuk, A. M., & Lyutyi, V. M. 1973, *Astrophys. Lett.*, 13, 165
- Cackett, E. M., Horne, K., & Winkler, H. 2007, *MNRAS*, 380, 669
- Cackett, E. M., Chiang, C.-Y., McHardy, I., et al. 2018, *ApJ*, 857, 53
- Collier, S. J., Horne, K., Kaspi, S., et al. 1998, *ApJ*, 500, 162
- Czerny, B., & Hryniewicz, K. 2011, *A&A*, 525, L8
- Czerny, B. 2014, 40th COSPAR Scientific Assembly, 40, E1.19-10-14
- Davidson, K., & Netzer, H. 1979, *Reviews of Modern Physics*, 51, 715
- Davis, S. W., Woo, J.-H., & Blaes, O. M. 2007, *ApJ*, 668, 682
- Davis, S. W., & Laor, A. 2011, *ApJ*, 728, 98
- Du, P., Hu, C., Lu, K.-X., et al. 2014, *ApJ*, 782, 45
- Du, P., Lu, K.-X., Zhang, Z.-X., et al. 2016, *ApJ*, 825, 126
- Event Horizon Telescope Collaboration, Akiyama, K., Alberdi, A., et al. 2019, *ApJ*, 875, L4
- Edelson, R. A. & Krolik, J. H. 1988, *ApJ*, 333, 646
- Edelson, R., Gelbord, J. M., Horne, K., et al. 2015, *ApJ*, 806, 129
- Edelson, R., Gelbord, J., Cackett, E., et al. 2019, *ApJ*, 870, 123
- Edelson, R., Gelbord, J., Cackett, E., et al. 2017, *ApJ*, 840, 41
- Esser, J., Pott, J.-U., Landt, H., & Vacca, W. D. 2019, *A&A*, 621, A46
- Fausnaugh, M. M., Denney, K. D., Barth, A. J., et al. 2016, *ApJ*, 821, 56
- Fausnaugh, M. M., Starkey, D. A., Horne, K., et al. 2018, *ApJ*, 854, 107
- Feng, H., Shen, Y., & Li, H. 2014, *ApJ*, 794, 77
- Gaskell, C. M., & Sparke, L. S. 1986, *ApJ*, 305, 175
- Gaskell, C. M., & Peterson, B. M. 1987, *ApJS*, 65, 1
- Gaskell, C. M., Goosmann, R. W., Antonucci, R. R. J., & Whysong, D. H. 2004, *ApJ*, 616, 147
- Gaskell, C. M. 2007, *The Central Engine of Active Galactic Nuclei*, 596
- Gaskell, C. M., & Benker, A. J. 2007, *arXiv:0711.1013*
- Gaskell, C. M. 2017, *MNRAS*, 467, 226
- Goad, M. R., Korista, K. T., & Ruff, A. J. 2012, *MNRAS*, 426, 3086
- Gravity Collaboration, Sturm, E., Dexter, J., et al. 2018, *Nature*, 563, 657
- Glass, I. S. 2004, *MNRAS*, 350, 1049
- Grier, C. J., Peterson, B. M., Pogge, R. W., et al. 2012, *ApJ*, 755, 60
- Haas, M., Chini, R., Ramolla, M., et al. 2011, *A&A*, 535, A73
- Ho, L. C., & Kim, M. 2015, *ApJ*, 809, 123
- Huchra, J., Latham, D. W., da Costa, L. N., Pellegrini, P. S., & Willmer, C. N. A. 1993, *AJ*, 105, 1637
- Isobe, T., Feigelson, E. D., Akritas, M. G., & Babu, G. J. 1990, *ApJ*, 364, 104
- Jiang, Y.-F., Green, P. J., Greene, J. E., et al. 2017, *ApJ*, 836, 186
- Kaspi, S., Smith, P. S., Netzer, H., et al. 2000, *ApJ*, 533, 631
- Kaasra, J. S., Petrucci, P.-O., Cappi, M., et al. 2011, *A&A*, 534, A36.
- Kinney, A. L., Calzetti, D., Bohlin, R. C., et al. 1996, *ApJ*, 467, 38
- Kishimoto, M., Antonucci, R., Blaes, O., et al. 2008, *Nature*, 454, 492
- Kokubo, M., Morokuma, T., Minezaki, T., et al. 2014, *ApJ*, 783, 46
- Landolt, A. U. 2009, *AJ*, 137, 4186
- Lang, D., Hogg, D. W., Mierle, K., Blanton, M., & Roweis, S. 2010, *AJ*, 139, 1782
- Liu, H. T., Bai, J. M., Zhao, X. H., & Ma, L. 2008, *ApJ*, 677, 884
- McLure, R. J., & Dunlop, J. S. 2004, *MNRAS*, 352, 1390
- Mehdipour, M., Branduardi-Raymont, G., Kaastra, J. S., et al. 2011, *A&A*, 534, A39
- Morgan, C. W., Kochanek, C. S., Morgan, N. D., & Falco, E. E. 2010, *ApJ*, 712, 1129
- Mosquera, A. M., Kochanek, C. S., Chen, B., et al. 2013, *ApJ*, 769, 53
- Mudd, D., Martini, P., Zu, Y., et al. 2018, *ApJ*, 862, 123
- Netzer, H. 2013, *The Physics and Evolution of Active Galactic Nuclei*, by Hagai Netzer, Cambridge, UK: Cambridge University Press, 2013,
- Netzer, H. 2015, *ARA&A*, 53, 365
- Oknyanskij, V. L., Horne, K., Lyuty, V. M., et al. 2003, *Active Galactic Nuclei: From Central Engine to Host Galaxy*, 290, 119
- Onken, C. A., Ferrarese, L., Merritt, D., et al. 2004, *ApJ*, 615, 645
- Park, D., Barth, A. J., Woo, J.-H., et al. 2017, *ApJ*, 839, 93
- Pelt, J., Hoff, W., Kayser, R., Refsdal, S., & Schramm, T. 1994, *A&A*, 286, 775
- Peterson, B. M. 1993, *PASP*, 105, 247
- Peterson, B. M., Ferrarese, L., Gilbert, K. M., et al. 2004, *ApJ*, 613, 682
- Pooley, D., Blackburne, J. A., Rappaport, S., et al. 2006, *ApJ*, 648, 67
- Pooley, D., Blackburne, J. A., Rappaport, S., & Schechter, P. L. 2007, *ApJ*, 661, 19
- Pozo Nuñez, F., Ramolla, M., Westhues, C., et al. 2012, *A&A*, 545, A84
- Pozo Nuñez, F., Haas, M., Chini, R., et al. 2014, *A&A*, 561, L8
- Pozo Nuñez, F., Haas, M., Ramolla, M., et al. 2014, *A&A*, 568, A36
- Pozo Nuñez, F., Ramolla, M., Westhues, C., et al. 2015, *A&A*, 576, A73
- Pozo Nuñez, F., Chelouche, D., Kaspi, S., & Niv, S. 2017, *PASP*, 129, 094101
- Ramolla, M., Haas, M., Westhues, C., et al. 2018, *A&A*, 620, A137
- Sakata, Y., Minezaki, T., Yoshii, Y., et al. 2010, *ApJ*, 711, 461
- Schlafly, E. F., & Finkbeiner, D. P. 2011, *ApJ*, 737, 103
- Sergeev, S. G., Doroshenko, V. T., Golubinskiy, Y. V., Merkulova, N. I., & Sergeeva, E. A. 2005, *ApJ*, 622, 129
- Shakura, N. I., & Sunyaev, R. A. 1973, *A&A*, 24, 337
- Shankar, F., Weinberg, D. H., & Miralda-Escudé, J. 2009, *ApJ*, 690, 20
- Shankar, F., Calderone, G., Knigge, C., et al. 2016, *ApJ*, 818, L1
- Shappee, B. J., Prieto, J. L., Grupe, D., et al. 2014, *ApJ*, 788, 48
- Schnülle, K., Pott, J.-U., Rix, H.-W., et al. 2015, *A&A*, 578, A57
- Tilton, E. M., & Shull, J. M. 2013, *ApJ*, 774, 67
- Wanders, I., Peterson, B. M., Alloin, D., et al. 1997, *ApJS*, 113, 69
- Welsh, W. F. 1999, *PASP*, 111, 1347
- Winkler, H., Glass, I. S., van Wyk, F., et al. 1992, *MNRAS*, 257, 659

APPENDIX A: .

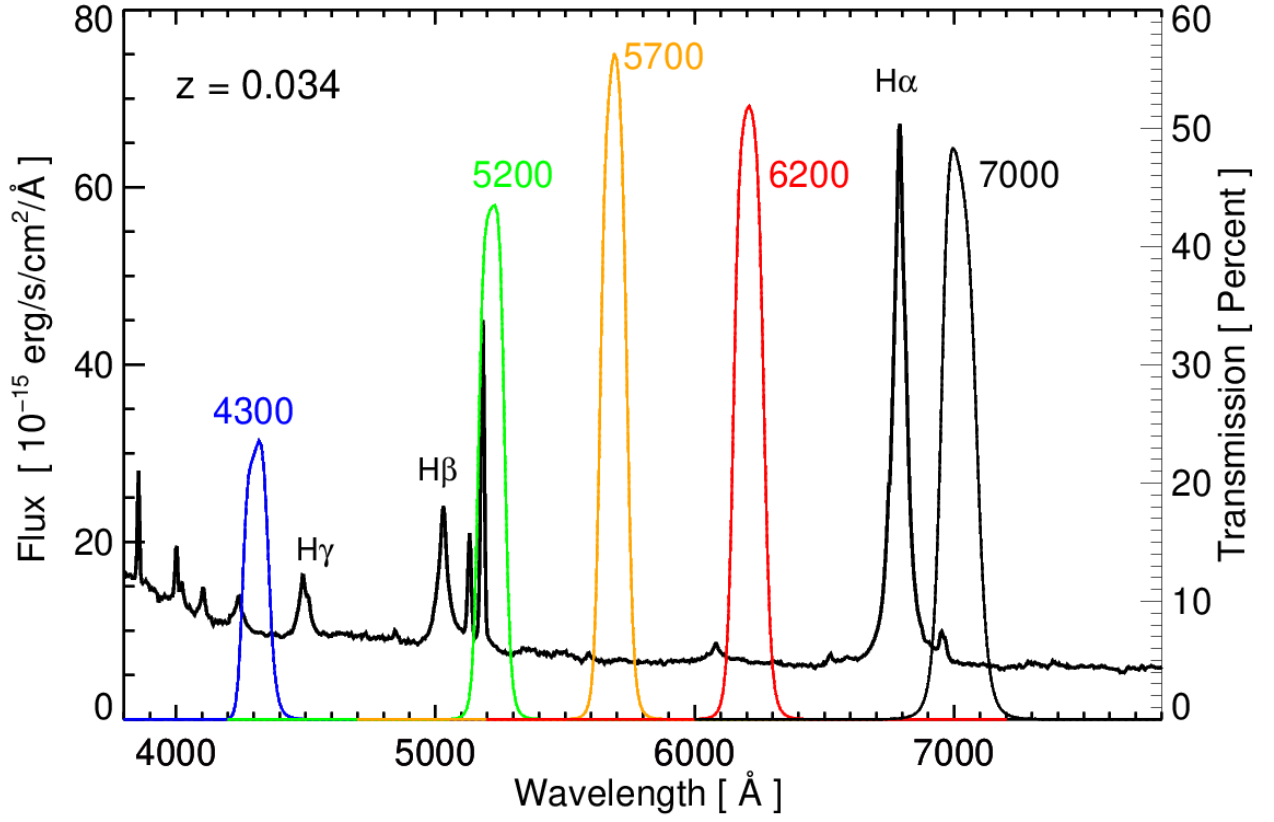


Figure A1. AGN Watch spectrum of Mrk509. The effective transmission of the narrow-band filters used in the monitoring are overplotted in colored lines. The filters curves have been folded with the quantum efficiency of the STL-6303 CCD camera.

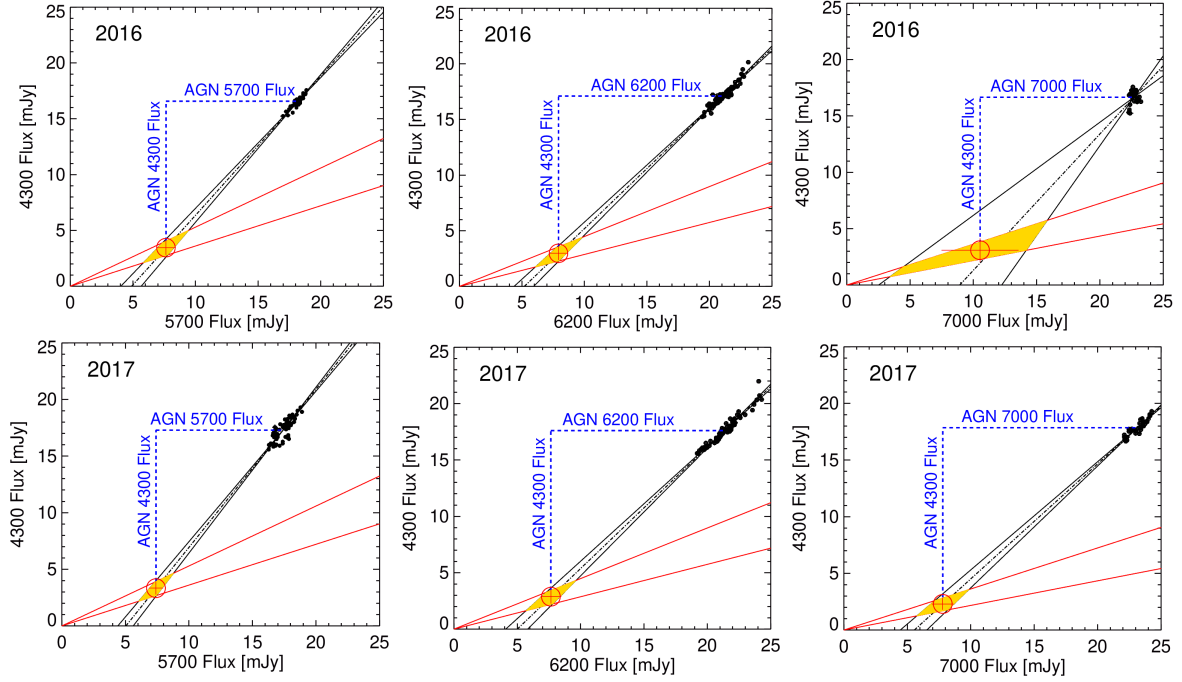


Figure A2. Flux variation gradient diagrams for 2016 (top) and 2017 (bottom) campaigns. The solid black lines delineate the ordinary least square bisector regression model yielding the range of the AGN slope. The red solid lines indicate the range of host slopes obtained from [Sakata et al. 2010](#) for a sample of 11 nearby Seyfert-1 galaxies. The intersection between the host galaxy and AGN slope (yellow area) gives the host galaxy flux in both bands (red circle with cross). The dash-dotted blue lines depict the range of the host subtracted AGN flux in both bands.

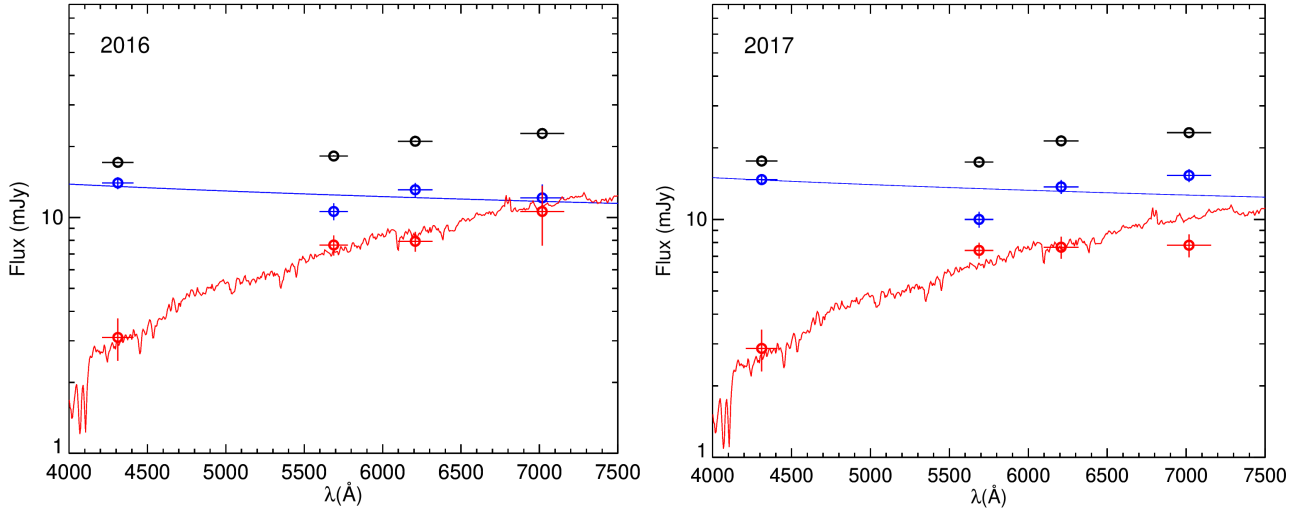


Figure A3. Flux decomposition as obtained from the FVG analysis for epochs 2016 (top) and 2017 (bottom). The total fluxes are shown with black circles. The host galaxy subtracted AGN spectrum (blue circles) is consistent with a blue AGN spectrum and follows the accretion disk [Shakura & Sunyaev 1973](#) model ($F_{\nu} \propto \nu^{1/3}$; blue line). A bulge model template of [Kinney et al. 1996](#) (red line) is a good fit to the host galaxy fluxes derived by the FVG analysis (red circles).

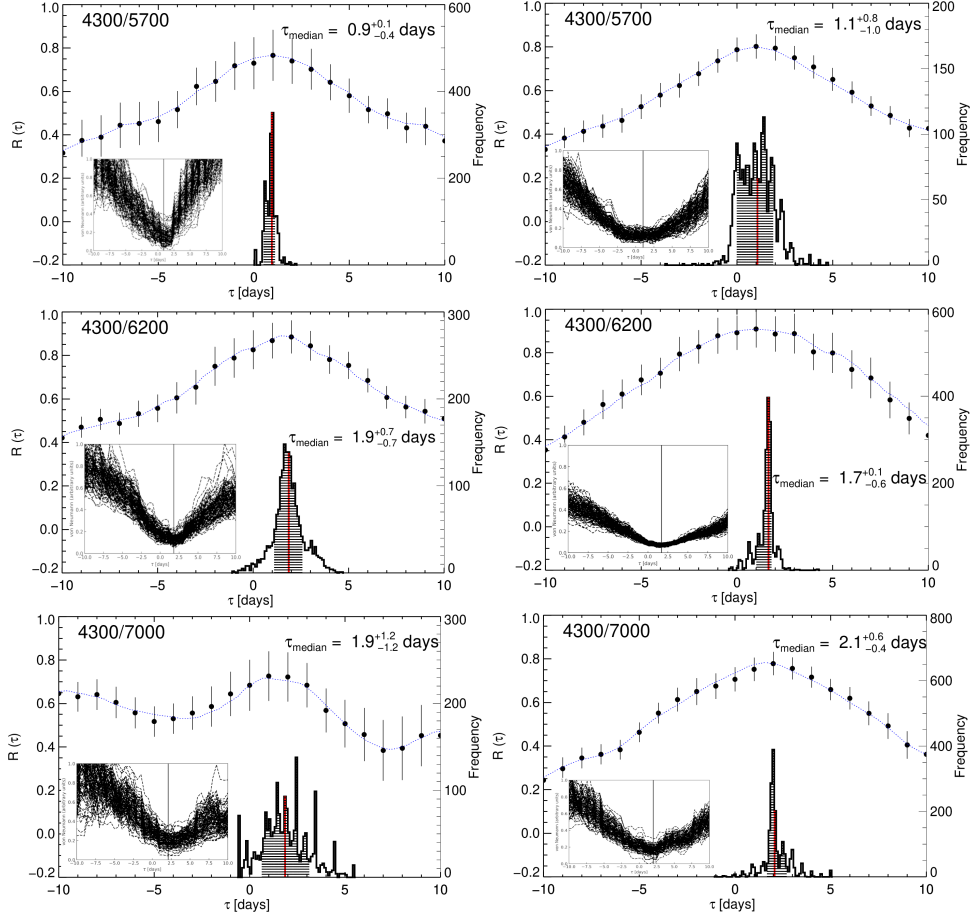


Figure A4. Results of the time delay analysis for 2016 (left) and 2017 (right) campaigns. The interpolated cross correlation function (ICCF) is shown as blue dotted lines, while the discrete correlation function (DCF) is shown as black circles with $\pm 1\sigma$ error bars. The histograms shows the distribution of the centroid time delay obtained by cross correlating 2000 flux randomized and randomly selected subset light curves (FR/RSS method). The black area marks the 68% confidence range used to calculate the errors of the centroid (red line). The inset shows the von Neumann (VN) estimator obtained for 2000 FR/RSS subset light curves.

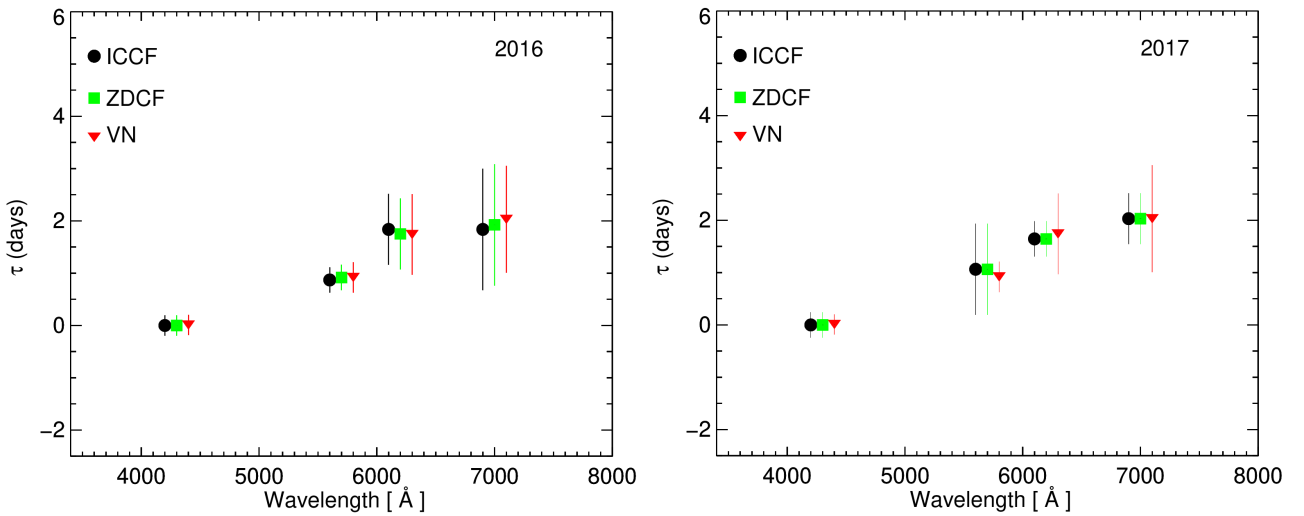


Figure A5. Time delay as a function of wavelength obtained for campaigns 2016 (left) and 2017 (right) using the ICCF (black circles), DCF (green squares) and von Neumann (red triangles) methods. The time delays are calculated with respect to the 4300 Å narrow-band and are corrected by the time dilation factor ($1+z = 1.0344$).

This paper has been typeset from a $\text{T}_\text{E}\text{X}/\text{L}^\text{A}\text{T}_\text{E}\text{X}$ file prepared by the author.

Table A1. NB4300, NB5700, NB6200 and NB7000 fluxes corrected by extinction for 2016 campaign. MJD correspond to the modified Julian Date (JD) JD-2,450,000. The fluxes are given in mJy.

MJD	F_{4300}	MJD	F_{5700}	MJD	F_{6200}	MJD	F_{7000}
57547.957	17.222 ± 0.154	57630.738	18.135 ± 0.203	57525.035	20.712 ± 0.168	57645.715	22.376 ± 0.250
57551.008	17.301 ± 0.137	57632.754	17.932 ± 0.092	57542.984	20.270 ± 0.210	57646.715	22.285 ± 0.204
57551.961	17.239 ± 0.120	57633.738	17.895 ± 0.092	57547.961	20.270 ± 0.210	57647.715	22.331 ± 0.159
57552.961	17.154 ± 0.103	57634.777	17.950 ± 0.092	57551.016	21.112 ± 0.105	57648.711	22.376 ± 0.113
57553.945	17.085 ± 0.103	57635.781	17.913 ± 0.092	57551.965	21.069 ± 0.105	57650.738	22.716 ± 0.113
57555.941	16.965 ± 0.103	57636.770	17.766 ± 0.092	57552.969	20.901 ± 0.105	57652.746	23.057 ± 0.113
57556.938	16.897 ± 0.103	57637.746	17.581 ± 0.092	57553.953	20.901 ± 0.105	57653.738	23.080 ± 0.113
57557.934	16.811 ± 0.103	57639.727	17.470 ± 0.092	57555.949	20.754 ± 0.105	57654.707	23.238 ± 0.113
57558.938	16.863 ± 0.120	57643.711	17.230 ± 0.166	57556.941	20.859 ± 0.105	57655.785	22.943 ± 0.113
57559.941	16.777 ± 0.154	57645.711	16.990 ± 0.203	57557.938	20.775 ± 0.105	57658.703	22.989 ± 0.113
57561.914	16.777 ± 0.137	57646.711	17.378 ± 0.185	57558.945	20.754 ± 0.105	57659.703	22.989 ± 0.113
57562.973	16.897 ± 0.137	57647.711	17.766 ± 0.148	57559.945	20.691 ± 0.168	57660.703	23.125 ± 0.113
57563.953	16.811 ± 0.103	57648.707	18.061 ± 0.111	57561.922	20.565 ± 0.252	57661.703	22.921 ± 0.113
57564.945	16.948 ± 0.103	57650.730	18.190 ± 0.092	57562.980	20.607 ± 0.252	57662.699	22.807 ± 0.113
57565.922	16.948 ± 0.103	57652.738	18.356 ± 0.092	57563.961	20.607 ± 0.189	57663.699	22.558 ± 0.113
57567.961	17.410 ± 0.103	57653.734	18.320 ± 0.092	57564.953	20.922 ± 0.105	57664.746	22.626 ± 0.113
57568.895	17.359 ± 0.086	57654.703	18.227 ± 0.092	57565.930	20.943 ± 0.105	57665.699	22.648 ± 0.113
57569.949	17.427 ± 0.086	57655.777	18.116 ± 0.092	57567.969	21.343 ± 0.105	57666.699	22.580 ± 0.113
57570.922	17.222 ± 0.086	57658.699	18.227 ± 0.092	57568.902	21.448 ± 0.105	57667.738	22.421 ± 0.136
57571.930	17.188 ± 0.086	57659.699	18.356 ± 0.092	57569.953	21.700 ± 0.105	57668.723	22.308 ± 0.113
57572.902	17.034 ± 0.086	57660.695	18.024 ± 0.092	57570.930	21.763 ± 0.105	57670.750	22.376 ± 0.159
57574.891	16.897 ± 0.086	57661.695	18.135 ± 0.092	57571.938	21.742 ± 0.105	57672.695	22.376 ± 0.182
57575.922	16.914 ± 0.086	57662.695	18.301 ± 0.092	57572.910	21.532 ± 0.105	57673.723	22.648 ± 0.159
57576.895	16.743 ± 0.086	57663.695	18.209 ± 0.111	57574.895	20.880 ± 0.105	57674.691	22.489 ± 0.136
57578.891	17.017 ± 0.103	57664.742	18.098 ± 0.092	57575.930	20.775 ± 0.105	57675.691	22.830 ± 0.136
57579.902	17.136 ± 0.103	57665.691	18.320 ± 0.092	57576.902	20.880 ± 0.105	57677.703	22.853 ± 0.113
57580.895	17.496 ± 0.103	57666.695	18.393 ± 0.092	57578.898	21.090 ± 0.105	57679.688	22.603 ± 0.113
57581.906	17.598 ± 0.103	57667.734	18.597 ± 0.092	57579.906	21.217 ± 0.105	57680.691	22.580 ± 0.136
57582.871	17.598 ± 0.103	57668.715	18.338 ± 0.111	57580.902	21.364 ± 0.105	57681.688	22.603 ± 0.113
57583.941	17.667 ± 0.103	57670.746	18.338 ± 0.148	57581.914	21.469 ± 0.105	57683.684	22.648 ± 0.113
57584.871	17.547 ± 0.086	57672.688	18.560 ± 0.166	57582.879	21.532 ± 0.105	57684.684	22.853 ± 0.113
57585.895	17.615 ± 0.086	57673.719	18.652 ± 0.148	57583.949	21.532 ± 0.126	57687.684	22.966 ± 0.159
57588.883	17.701 ± 0.103	57674.688	18.615 ± 0.148	57584.879	21.532 ± 0.126	-	-
57591.844	17.906 ± 0.086	57675.688	18.615 ± 0.148	57585.902	21.532 ± 0.189	-	-
57593.844	17.838 ± 0.034	57677.699	18.597 ± 0.111	57588.891	21.574 ± 0.210	-	-
57594.891	17.957 ± 0.120	57679.684	18.726 ± 0.092	57591.852	21.763 ± 0.189	-	-
57595.840	17.974 ± 0.137	57680.688	18.763 ± 0.092	57593.848	21.932 ± 0.126	-	-
57596.848	18.265 ± 0.137	57681.680	18.855 ± 0.092	57594.895	22.100 ± 0.105	-	-
57597.844	18.573 ± 0.103	57683.680	18.763 ± 0.092	57595.848	22.247 ± 0.105	-	-
57599.832	18.556 ± 0.103	57684.680	18.597 ± 0.092	57597.848	22.394 ± 0.105	-	-
57600.816	18.351 ± 0.103	57685.680	18.800 ± 0.092	57599.840	22.331 ± 0.105	-	-
57602.812	17.752 ± 0.137	57687.680	18.818 ± 0.148	57600.824	22.058 ± 0.105	-	-
57603.855	17.359 ± 0.103	-	-	57602.816	21.826 ± 0.105	-	-
57604.809	17.188 ± 0.137	-	-	57603.863	21.574 ± 0.105	-	-
57605.797	16.863 ± 0.137	-	-	57604.816	21.406 ± 0.105	-	-
57611.820	16.640 ± 0.137	-	-	57605.805	21.006 ± 0.105	-	-
57616.750	16.384 ± 0.137	-	-	57611.828	20.838 ± 0.126	-	-
57626.770	16.658 ± 0.103	-	-	57616.758	20.397 ± 0.147	-	-
57630.727	16.640 ± 0.103	-	-	57630.734	20.670 ± 0.126	-	-
57632.742	16.623 ± 0.103	-	-	57632.750	20.586 ± 0.105	-	-
57633.727	16.487 ± 0.103	-	-	57633.734	20.670 ± 0.105	-	-
57634.766	16.452 ± 0.103	-	-	57634.773	20.586 ± 0.105	-	-
57635.770	16.316 ± 0.103	-	-	57635.777	20.397 ± 0.105	-	-
57636.762	16.179 ± 0.103	-	-	57636.766	20.334 ± 0.105	-	-
57637.734	16.110 ± 0.137	-	-	57637.742	20.102 ± 0.105	-	-
57639.715	15.854 ± 0.086	-	-	57639.719	19.976 ± 0.105	-	-
57643.703	15.649 ± 0.086	-	-	57643.707	19.598 ± 0.126	-	-
57645.703	15.238 ± 0.086	-	-	57645.707	19.429 ± 0.168	-	-
57646.699	15.306 ± 0.086	-	-	57646.707	19.577 ± 0.168	-	-
57647.699	15.546 ± 0.086	-	-	57647.703	20.144 ± 0.126	-	-
57648.695	16.008 ± 0.120	-	-	57648.703	20.207 ± 0.105	-	-

Table A1 – *continued*

MJD	F_{4300}	MJD	F_{5700}	MJD	F_{6200}	MJD	F_{7000}
57650.719	16.298 ± 0.120	-	-	57650.727	20.186 ± 0.126	-	-
57652.727	16.418 ± 0.120	-	-	57652.734	19.997 ± 0.126	-	-
57653.723	16.401 ± 0.120	-	-	57653.730	19.976 ± 0.126	-	-
57654.691	16.264 ± 0.103	-	-	57654.699	19.850 ± 0.126	-	-
57655.770	16.247 ± 0.103	-	-	57655.773	19.892 ± 0.105	-	-
57658.688	16.367 ± 0.103	-	-	57658.695	20.249 ± 0.105	-	-
57659.688	16.469 ± 0.120	-	-	57659.695	20.565 ± 0.105	-	-
57660.688	16.675 ± 0.120	-	-	57660.691	20.544 ± 0.126	-	-
57661.688	16.623 ± 0.120	-	-	57661.691	20.523 ± 0.147	-	-
57662.684	16.743 ± 0.120	-	-	57662.691	20.481 ± 0.105	-	-
57663.684	16.640 ± 0.120	-	-	57663.691	20.565 ± 0.105	-	-
57664.684	16.743 ± 0.120	-	-	57664.691	20.565 ± 0.126	-	-
57665.684	16.777 ± 0.103	-	-	57665.688	20.733 ± 0.126	-	-
57666.684	16.709 ± 0.103	-	-	57666.691	20.586 ± 0.105	-	-
57667.723	16.829 ± 0.120	-	-	57667.727	20.523 ± 0.126	-	-
57668.707	16.829 ± 0.120	-	-	57668.711	20.565 ± 0.105	-	-
57670.734	16.914 ± 0.120	-	-	57670.742	20.586 ± 0.126	-	-
57672.680	16.931 ± 0.103	-	-	57672.684	20.712 ± 0.147	-	-
57673.707	17.154 ± 0.103	-	-	57673.711	20.670 ± 0.126	-	-
57674.676	17.256 ± 0.103	-	-	57674.680	20.859 ± 0.105	-	-
57675.676	17.188 ± 0.103	-	-	57675.680	20.859 ± 0.105	-	-
57677.688	17.290 ± 0.120	-	-	57677.691	21.112 ± 0.105	-	-
57678.672	17.171 ± 0.120	-	-	57678.680	20.985 ± 0.105	-	-
57679.672	17.188 ± 0.103	-	-	57679.680	21.154 ± 0.126	-	-
57680.676	17.239 ± 0.120	-	-	57680.684	21.006 ± 0.105	-	-
57681.672	17.564 ± 0.103	-	-	57681.676	21.427 ± 0.105	-	-
57683.668	17.188 ± 0.120	-	-	57683.676	21.553 ± 0.126	-	-
57684.668	17.068 ± 0.103	-	-	57684.676	21.427 ± 0.105	-	-
57685.668	17.273 ± 0.103	-	-	57685.676	21.658 ± 0.126	-	-
57692.703	18.231 ± 0.120	-	-	57687.672	21.995 ± 0.105	-	-
57694.664	18.847 ± 0.120	-	-	57692.711	22.478 ± 0.105	-	-
57695.699	19.018 ± 0.120	-	-	57694.672	22.752 ± 0.126	-	-
57696.660	19.086 ± 0.120	-	-	57695.707	22.647 ± 0.105	-	-
57698.660	19.497 ± 0.120	-	-	57696.668	22.562 ± 0.105	-	-
57699.664	20.146 ± 0.103	-	-	57698.668	22.668 ± 0.126	-	-
-	-	-	-	57699.672	23.109 ± 0.126	-	-

Table A2. The same as Table A1 but for 2017 campaign.

MJD	F_{4300}	MJD	F_{5700}	MJD	F_{6200}	MJD	F_{7000}
57900.988	21.978 ± 0.123	57917.930	17.643 ± 0.1923	57900.996	24.053 ± 0.128	57965.840	22.311 ± 0.114
57904.961	20.713 ± 0.105	57920.992	18.062 ± 0.0872	57904.969	24.117 ± 0.107	57966.820	22.129 ± 0.114
57907.008	20.362 ± 0.088	57921.957	17.643 ± 0.0872	57907.016	24.288 ± 0.107	57967.848	22.220 ± 0.114
57907.988	20.327 ± 0.105	57922.938	17.818 ± 0.0872	57907.996	23.903 ± 0.107	57968.832	22.152 ± 0.114
57909.004	19.923 ± 0.105	57923.953	18.027 ± 0.0872	57909.012	23.689 ± 0.107	57969.828	22.107 ± 0.136
57910.004	19.413 ± 0.088	57924.953	17.922 ± 0.0872	57910.012	23.561 ± 0.107	57970.844	22.311 ± 0.227
57910.934	19.009 ± 0.123	57925.926	17.853 ± 0.0872	57910.945	22.984 ± 0.128	57971.836	22.107 ± 0.114
57911.934	18.746 ± 0.088	57929.914	17.591 ± 0.0872	57911.941	22.599 ± 0.107	57973.852	22.629 ± 0.159
57913.012	18.113 ± 0.123	57930.930	17.713 ± 0.0876	57913.020	22.150 ± 0.171	57974.809	22.993 ± 0.136
57915.957	17.164 ± 0.123	57931.934	17.818 ± 0.0873	57917.922	21.231 ± 0.214	57975.801	23.288 ± 0.136
57917.914	17.358 ± 0.123	57932.906	17.818 ± 0.0875	57920.988	21.530 ± 0.107	57976.828	23.220 ± 0.136
57920.980	17.867 ± 0.088	57933.938	17.870 ± 0.0878	57921.953	21.102 ± 0.107	57977.840	23.311 ± 0.136
57921.941	17.358 ± 0.105	57935.895	17.382 ± 0.0701	57922.934	21.209 ± 0.107	57978.883	23.743 ± 0.136
57922.922	17.463 ± 0.088	57936.965	17.382 ± 0.0872	57923.949	21.252 ± 0.107	57979.852	23.834 ± 0.136
57923.941	17.727 ± 0.088	57937.957	17.138 ± 0.0872	57924.945	21.316 ± 0.107	57982.805	23.606 ± 0.136
57924.938	17.692 ± 0.105	57938.902	16.824 ± 0.0872	57925.922	21.594 ± 0.107	57983.801	23.379 ± 0.114
57925.910	17.463 ± 0.088	57939.902	16.876 ± 0.1572	57929.910	20.717 ± 0.107	57987.754	23.515 ± 0.136
57926.895	17.129 ± 0.123	57951.871	16.650 ± 0.1052	57930.922	20.760 ± 0.107	57988.797	23.652 ± 0.114
57929.902	16.690 ± 0.088	57952.859	16.284 ± 0.0872	57931.926	20.717 ± 0.107	57989.785	23.902 ± 0.114
57930.914	16.637 ± 0.088	57953.902	16.284 ± 0.1222	57932.902	20.696 ± 0.107	57990.738	24.015 ± 0.159
57931.918	16.848 ± 0.088	57956.848	16.301 ± 0.1222	57933.934	20.568 ± 0.107	57991.797	24.106 ± 0.114
57932.895	16.743 ± 0.088	57957.836	16.458 ± 0.1052	57935.887	20.162 ± 0.107	57992.797	24.265 ± 0.136
57933.926	16.514 ± 0.105	57958.848	16.440 ± 0.1222	57936.961	19.991 ± 0.107	57993.793	24.129 ± 0.114
57935.879	16.268 ± 0.088	57959.824	16.667 ± 0.1391	57937.949	19.755 ± 0.107	57995.789	23.652 ± 0.136
57936.953	16.110 ± 0.088	57960.871	16.894 ± 0.0872	57938.895	19.713 ± 0.107	57996.789	23.629 ± 0.136
57937.941	15.917 ± 0.088	57961.828	16.981 ± 0.0872	57939.895	19.841 ± 0.171	57997.789	23.584 ± 0.227
57938.887	15.917 ± 0.105	57962.855	16.946 ± 0.0872	57951.863	19.371 ± 0.107	57999.789	23.447 ± 0.136
57939.887	16.023 ± 0.123	57963.828	16.981 ± 0.1052	57952.852	19.199 ± 0.128	58000.793	23.402 ± 0.114
57951.855	15.829 ± 0.105	57964.879	16.754 ± 0.1221	57953.898	19.285 ± 0.128	58003.727	23.016 ± 0.159
57952.844	15.583 ± 0.105	57965.832	16.737 ± 0.0878	57956.840	19.542 ± 0.128	58004.727	22.743 ± 0.114
57953.891	15.636 ± 0.123	57966.816	16.597 ± 0.1056	57957.832	19.627 ± 0.128	58006.727	22.470 ± 0.136
57956.832	15.987 ± 0.123	57967.840	16.702 ± 0.1228	57958.840	19.755 ± 0.107	58007.801	22.470 ± 0.136
57957.824	16.093 ± 0.123	57968.828	16.876 ± 0.1058	57959.816	19.862 ± 0.107	58008.723	22.698 ± 0.136
57958.832	16.110 ± 0.141	57969.820	16.667 ± 0.1058	57960.863	19.884 ± 0.107	58009.723	22.925 ± 0.114
57959.809	16.110 ± 0.176	57970.840	16.650 ± 0.1741	57961.820	20.247 ± 0.128	58016.715	22.947 ± 0.114
57960.855	16.497 ± 0.105	57971.828	16.719 ± 0.1392	57962.852	20.696 ± 0.128	58017.715	22.993 ± 0.114
57961.812	16.673 ± 0.123	57973.848	16.772 ± 0.2092	57963.824	20.889 ± 0.128	-	-
57962.844	16.954 ± 0.123	57974.801	16.911 ± 0.1922	57964.875	20.675 ± 0.128	-	-
57963.816	16.813 ± 0.105	57975.797	17.120 ± 0.1052	57965.824	20.717 ± 0.128	-	-
57964.863	16.655 ± 0.158	57976.824	17.190 ± 0.1572	57966.809	20.803 ± 0.150	-	-
57965.816	16.743 ± 0.105	57977.836	17.556 ± 0.1222	57967.836	20.782 ± 0.128	-	-
57966.801	16.813 ± 0.105	57978.875	17.748 ± 0.1058	57968.820	20.846 ± 0.128	-	-
57967.828	16.655 ± 0.123	57979.844	18.027 ± 0.1220	57969.816	20.889 ± 0.150	-	-
57968.812	16.831 ± 0.123	57982.797	17.765 ± 0.1221	57970.832	20.995 ± 0.214	-	-
57969.809	17.042 ± 0.105	57983.793	17.905 ± 0.1223	57971.820	21.102 ± 0.214	-	-
57970.824	17.024 ± 0.176	57987.750	18.149 ± 0.1222	57973.840	21.081 ± 0.192	-	-
57971.812	17.217 ± 0.176	57988.789	18.097 ± 0.1051	57974.797	20.974 ± 0.128	-	-
57973.832	17.551 ± 0.228	57989.781	18.323 ± 0.1050	57975.789	20.953 ± 0.107	-	-
57974.789	17.358 ± 0.211	57990.734	18.480 ± 0.1053	57976.816	21.166 ± 0.107	-	-
57975.781	17.323 ± 0.105	57991.789	18.550 ± 0.1222	57977.828	21.487 ± 0.128	-	-
57976.809	17.815 ± 0.123	57992.789	18.777 ± 0.1391	57978.871	22.107 ± 0.128	-	-
57977.820	18.236 ± 0.105	57993.785	18.899 ± 0.1222	57979.840	22.086 ± 0.128	-	-
57978.863	18.201 ± 0.105	57995.785	18.341 ± 0.1570	57982.789	22.064 ± 0.128	-	-
57979.832	18.377 ± 0.123	57996.785	18.271 ± 0.1741	57983.785	22.043 ± 0.128	-	-
57982.781	18.271 ± 0.105	57997.781	17.783 ± 0.1741	57987.742	21.808 ± 0.107	-	-
57983.777	18.570 ± 0.123	57999.781	17.678 ± 0.1570	57988.785	21.979 ± 0.128	-	-
57987.734	18.658 ± 0.123	58000.785	17.556 ± 0.1742	57989.773	22.107 ± 0.128	-	-
57988.777	18.394 ± 0.105	58003.723	17.452 ± 0.1573	57990.727	22.150 ± 0.107	-	-
57989.766	18.377 ± 0.123	58004.723	17.469 ± 0.2094	57991.781	22.364 ± 0.128	-	-
57990.719	18.658 ± 0.088	58006.719	17.417 ± 0.1742	57992.781	22.471 ± 0.107	-	-
57991.773	19.009 ± 0.123	58007.793	17.469 ± 0.1051	57993.781	22.556 ± 0.107	-	-
57992.773	19.290 ± 0.088	58008.719	17.469 ± 0.1051	57995.777	22.193 ± 0.214	-	-
57993.770	18.904 ± 0.105	58009.715	17.609 ± 0.1740	57996.777	21.765 ± 0.150	-	-
57995.770	18.289 ± 0.123	58016.707	17.399 ± 0.1052	57997.777	21.808 ± 0.214	-	-

Table A2 – *continued*

MJD	F_{4300}	MJD	F_{5700}	MJD	F_{6200}	MJD	F_{7000}
57996.770	18.008 ± 0.123	58017.707	17.609 ± 0.1051	57999.773	21.915 ± 0.128	-	-
57997.770	18.025 ± 0.176	-	-	58000.777	21.765 ± 0.107	-	-
57999.766	17.920 ± 0.105	-	-	58003.715	21.530 ± 0.150	-	-
58000.770	17.674 ± 0.088	-	-	58004.715	21.658 ± 0.128	-	-
58003.707	17.569 ± 0.105	-	-	58006.711	21.765 ± 0.128	-	-
58004.707	17.692 ± 0.123	-	-	58007.789	21.787 ± 0.150	-	-
58006.703	17.533 ± 0.123	-	-	58008.711	21.851 ± 0.150	-	-
58007.781	17.727 ± 0.141	-	-	58009.711	21.872 ± 0.171	-	-
58008.703	17.744 ± 0.123	-	-	58016.703	21.551 ± 0.128	-	-
58009.703	17.674 ± 0.176	-	-	58017.703	21.637 ± 0.128	-	-
58016.695	17.621 ± 0.123	-	-	-	-	-	-
58017.695	17.621 ± 0.105	-	-	-	-	-	-